

Crude closure for flow with topography through large-scale statistical theory

M J Grote^{†§} and A J Majda[‡]

[†] Departement Mathematik, ETH Zürich, CH-8092 Zürich, Switzerland

[‡] Courant Institute of Mathematical Sciences, NYU, New York, NY 10012, USA

E-mail: grote@math.ethz.ch

Received 26 January 1999, in final form 28 July 1999

Recommended by G Morriss

Abstract. Crude closure algorithms based on equilibrium statistical theories are developed here for prototypical geophysical flows involving barotropic flow over topography. These algorithms are developed utilizing the simplest energy–enstrophy statistical theory for flow with topography. Only a single parameter, the energy, is tracked by the algorithm and the entire flow structure is predicted through the equilibrium statistical state. In particular, no explicit parametrization of a sub-grid scale energy spectrum is utilized in the algorithm. The predictions of the crude closure algorithm are compared with direct pseudo-spectral numerical simulations of the barotropic flow equations with random small-scale forcing and dissipation for a variety of random topographies in basin, channel and periodic geometries. In most situations studied here, the energy is tracked within small errors by the crude closure, while the velocity errors rarely exceed 10% provided that the enstrophy/energy ratio is not large or growing significantly in time. Examples are also introduced where the crude closure algorithm based on the energy–enstrophy theory fails; in these circumstances, a crude closure algorithm based on more sophisticated equilibrium statistical theories is introduced as a possible remedy.

AMS classification scheme numbers: 76F55, 86-08, 82-08, 82B21, 86A05

1. Introduction

The tendency of turbulent geophysical flows to display two-dimensional behaviour and self-organize into coherent structures has been reported numerous times from physical observations and numerical simulations [1, 2]. Various equilibrium statistical theories have been proposed to provide a mathematical framework underpinning the well known emergence of coherent structures in freely evolving two-dimensional flow. These theories apply to inviscid and unforced flow and attempt to predict the large-time behaviour as it approaches statistical equilibrium. Both the infinite number of degrees of freedom and the infinite number of conserved integrals preclude the direct use of classical statistical mechanics for a two-dimensional flow. As a result various statistical theories have been proposed, which differ from each other mainly by their individual choice of conserved quantities and the ‘discretization’ procedure used to represent the continuum by a countable set of ‘particles’ (spectral representation, point-vortices, lattice models, etc). Examples are the energy–enstrophy theory [3, 4], the point-vortex theory [5–8], the Miller–Robert

§ Author to whom correspondence should be addressed.

theory [9–11] and a very recent few-constraints statistical theory based on extrema of the potential vorticity [12, 13]. Each statistical theory yields a different relationship between the vorticity and the stream function, which defines a coarse-grained (macroscopic) description of the steady flow at statistical equilibrium, superimposed with local random fluctuations.

Rigorous theory [14] suggests that in some contexts it may be appropriate (and certainly more practical) to ignore all but a few of the infinitely many high-order enstrophy invariants when constructing a closure scheme. Furthermore, real flows are neither inviscid nor freely evolving, so that such higher-order equilibrium statistics based on inviscid dynamics are rapidly lost with time. Additional evidence is provided by a numerical study in [14], which shows that for a viscous decaying flow, even the simplest statistical theories accurately describe the overall evolution of the time-dependent flow. These encouraging results led the authors [15] to devise crude closure algorithms based on few-constraint statistical theories. These algorithms involve the nonlinear evolution of a few parameters, such as the energy and the circulation. They are designed through enforcing the following assumption:

The effect of small-scale forcing and dissipation is to change instantaneously the large-scale statistical structure to a new large-scale statistical structure with an adjusted energy and circulation.

Of course, in the postulates of crude closure listed above, we tacitly assume that the large scales respond on a longer time scale than the smaller spatial scale variations, i.e. there is scale separation in time. The crude closure algorithms displayed a remarkably accurate and robust predictive ability of the large-scale behaviour of a damped flow driven by small-scale random forcing in a basin, even under harsh conditions where all assumptions underlying equilibrium statistical theories are clearly violated [15] and without any turbulence parametrization for the inverse cascade process.

The development of crude closure models for fluid flows which exhibit organized large-scale structure, such as geophysical flows, remains an important practical issue. In particular, the evolution of large-scale ocean flows remains a formidable challenge and necessitates the modelling of unresolved eddy motion. Simulations by Holloway [16, 17] indicate that subscale modelling based on statistical mechanics leads to substantial improvement in model fidelity without incurring the cost of eddy resolution. Holloway suggests that the unresolved eddies are not a damping of the ocean circulation but rather a systematic driving force which tends to move the model to higher entropy states. In contrast, conventional eddy–viscosity models tend to drag the numerical solution toward a state of rest.

Barotropic flows over topography are the simplest prototype geophysical flows where even the simplest energy–enstrophy statistical theory yields striking predictions for a ‘most probable state’ mean flow [4, 18]. The emergence of such states as averages over large-time intervals in damped and driven numerical simulations has been studied extensively with many interesting results [1, 19–21]. Here, in a complementary direction, we devise and test crude closure algorithms based on the energy–enstrophy statistical theory, where the entire closure is based on a single predicted evolving parameter, the energy.

In section 2, we extend crude closure algorithms presented by the authors in [15] to barotropic flow over topography. The simplest algorithm involves the nonlinear evolution of a single parameter, the energy, for dynamic closure based on the energy–enstrophy statistical theory. Crude closure based on the inclusion of a second parameter, the circulation, is also presented. In section 3, we test the crude closure algorithms developed in section 2 on solutions of the barotropic flow equations over a random topography defined on a rectangular domain with stress-free boundary conditions and with strong small-scale forcing at moderately large

Reynolds numbers. We test the crude dynamic closure under increasingly stringent conditions ranging from freely decaying flows to spin-up from rest by random forcing with like-signed vortices, and finally to random forcing by vortices with alternating or opposite sign. We compare standard 128^2 spectral code numerical simulations with crude dynamic closure based upon only a single nonlinearly evolving parameter in the energy–enstrophy theory. Typically the energy is tracked with such accuracy, that the predicted value can hardly be distinguished from the exact energy. To demonstrate the greater versatility of two-parameter crude closure dynamics, we present in section 3.3 a situation of complete flow reversal, which cannot be predicted by the one-parameter crude closure algorithm. Here the inclusion of a second parameter, the circulation, in the crude closure provides the key to predicting the flow behaviour. In section 4 we perform a study analogous to that in section 3 but for flow in a channel. The numerical results corroborate the previous results and demonstrate the ability of the crude dynamic closure to cross violent changes in flow topology, as the flow reorganizes from a flow regime dominated by topography to a regime dominated by relative vorticity. Finally, in section 5, we point out the limitations of the crude closure based on the simple energy–enstrophy theory via a special low-energy dynamic transition over two-mode layered topography, which the algorithm fails to predict. Additional results suggest the potential benefit from using a recent more sophisticated statistical theory [12, 13], which involves only a few additional conserved quantities.

2. Crude closure dynamics

We consider the barotropic flow equations with damping and driving over topography [22] in a two-dimensional region Ω ,

$$\frac{\partial q}{\partial t} + \vec{v} \cdot \nabla q = P_0(\Delta)\omega + F. \quad (1)$$

Here $\vec{v}(x, y, t)$ denotes the velocity, $q(x, y, t)$ the potential vorticity and $\omega(x, y, t)$ the relative vorticity of the flow. They are related to each other via the stream function ψ by

$$\vec{v} = \nabla^\perp \psi = \left(-\frac{\partial \psi}{\partial y}, \frac{\partial \psi}{\partial x} \right) \quad (2)$$

$$\omega = \Delta \psi \quad (3)$$

$$q = \omega + h \quad (4)$$

where $h(x, y)$ defines the underlying topography. Dissipative effects are incorporated through the viscous operator $P_0(\Delta)$ defined by

$$P_0(\Delta)\omega = -d\omega + \nu\Delta\omega + \nu_H\Delta^3\omega. \quad (5)$$

The viscous operator includes the Ekman drag coefficient, d , the Newtonian viscosity coefficient, ν , and the hyperviscosity coefficient, ν_H . Higher-order effects could easily be incorporated. The first two dissipation mechanisms are radically different from each other. While Ekman drag models the effects of boundary layers in large-scale geophysical flows and dissipates energy at all scales equally, Newtonian viscosity corresponds to molecular or turbulent diffusion and dissipates the smaller scales much more strongly. Frequently used in geophysical applications, the main role of hyperviscosity in the present discussion is to guarantee numerical stability in situations where we set $\nu = 0$ in (5) (sections 3.4, 4.2 and

5.2). We choose the forcing F to mimic a random bombardment of the flow with localized smoothed vortices ω_r of radius r ,

$$F = \sum_{j \geq 1} \delta(t - t_j) \omega_r (\vec{x} - \vec{x}_j). \quad (6)$$

The precise definition of ω_r is given in (45).

The bounded domain Ω stands for the periodic box, the basin or the channel. If $\Omega = [0, 2\pi] \times [0, 2\pi]$ is the periodic box (torus), both ψ and h are 2π -periodic in x and y , and we assume that their integrals over Ω vanish. Alternatively, if $\Omega = [0, 2\pi] \times [0, \pi]$ is the channel, ψ and h are 2π -periodic in x and satisfy free-slip boundary conditions at the upper and lower boundaries $y = 0, \pi$,

$$\frac{\partial^{2p}}{\partial y^{2p}} \psi(x, y, t) = 0 \quad y = 0, \pi \quad p = 0, 1, 2, 3. \quad (7)$$

Finally, if $\Omega = [0, \pi] \times [0, \pi]$ is the basin, neither ψ nor h are periodic; hence, we impose free-slip boundary conditions over the entire boundary of Ω ,

$$\frac{\partial^{2p}}{\partial n^{2p}} \psi(x, y, t) = 0 \quad p = 0, 1, 2, 3 \quad (8)$$

where n is normal to the boundary of Ω . In the absence of topography and Ekman drag, $h(x, y) = 0$ and $d = 0$, the barotropic flow equations (1) reduce to the two-dimensional Navier–Stokes equations.

At any time t the energy E , the enstrophy \mathcal{E} and the circulation Γ are given by

$$E(t) = \frac{1}{2} \overline{\int} |\vec{v}|^2 = -\frac{1}{2} \overline{\int} \omega \psi \quad (9)$$

$$\mathcal{E}(t) = \frac{1}{2} \overline{\int} q^2 \quad (10)$$

$$\Gamma(t) = \overline{\int} q. \quad (11)$$

Here the horizontal bar across the integral sign indicates normalization with respect to the area of Ω . In the absence of forcing and viscous effects ($F = 0$ and $P_0(\Delta) \equiv 0$), the barotropic flow equations (1) conserve the energy, the enstrophy, the circulation, as well as the infinite number of integrals involving any arbitrary nonlinear function G of the potential vorticity,

$$\overline{\int} G(q). \quad (12)$$

Given a subset of conserved quantities what is the most probable flow configuration, q^* , at statistical equilibrium? Various statistical theories have been proposed to answer this question. These theories differ from each other through their individual choice of conserved quantities. Typically, they yield a nonlinear elliptic *mean-field equation*, which relates the coarse-grained potential vorticity field, q^* , to its corresponding stream function, ψ^* , via

$$q^* = f(\psi^*; E, \Gamma, \dots) \quad q^* = \Delta \psi^* + h. \quad (13)$$

The stream lines of these mean flows are smooth across Ω ; they ignore small-scale fluctuations and thus correspond to large-scale coherent structures in the flow. Because of topography they can contain small-scale features, in particular at low energy. Since equation (13) implies that

$$\nabla^\perp \psi^* \cdot \nabla q^* = 0 \quad (14)$$

any such mean flow is an exact steady-state solution of the inviscid and unforced barotropic flow equations (1).

2.1. Energy–enstrophy theories

The simplest non-trivial relation between q^* and ψ^* is linear and results from the energy–enstrophy theory for two-dimensional inviscid flow over topography. This equilibrium statistical theory starts from a truncated spectral representation of the equations of motion (1) in the absence of forcing and viscosity. Instead of the infinite number of conserved integrals in (12), the truncated dynamics then conserve only the energy and the enstrophy. By maximizing the entropy of this finite-dimensional dynamical system, Salmon *et al* [4] derive the mean-field equation

$$q^* = \mu \psi^* \quad (15)$$

where μ is the ratio of the Lagrange multipliers of the energy and the enstrophy. Since the integral of h vanishes, equation (15) has a unique solution for all $\mu > -\lambda_1$, where $\lambda_1 > 0$ is the lowest eigenvalue of the Laplacian in Ω —recall that zero is not an eigenvalue because we have assumed that the integral of ψ vanishes in periodic geometry. For a given energy there are, in general, multiple stationary solutions of (15) for different values of μ . Yet only the steady states that lie on the branch $\mu > -\lambda_1$ are nonlinearly stable and therefore they are the most physically relevant; they also minimize the potential enstrophy for a given energy [19]. Carnevale and Frederiksen [18] show that in the limit of infinite resolution the canonical equilibrium is statistically sharp and identical to the nonlinearly stable minimum enstrophy state. In summary, for every value of the energy $E > 0$ there is a unique value $\mu > -\lambda_1$, which determines the nonlinearly stable steady state via (15).

Let us assume that the flow is initially at statistical equilibrium, which is completely defined by its energy. As time progresses, the flow evolves under the constant action of small-scale forcing and dissipation. With the addition of every new localized vortex, the energy changes slightly, thereby forcing the large-scale flow into a new statistical state with adjusted energy. In the absence of forcing, the energy decreases because of dissipative effects; we estimate the decay in energy by assuming that all dissipation occurs in the large scales of the flow. This strategy leads to the crude closure algorithm, which captures the large-scale behaviour of the damped and driven flow only by tracking the energy without actually solving the fluid equations.

As the flow evolves under the constant bombardment with localized vortices, it alternates between two extreme flow regimes: a phase of applied forcing and a phase of pure decay.

Applied forcing

We begin with the addition of a single vortex ω at $t = \bar{t}$ to the current approximate state $\bar{\omega} = \bar{q} - h$ of the flow. Let \bar{t}_- denote the instant just before and \bar{t}_+ the instant right after the event. Then

$$\psi_{\bar{t}_+} = \bar{\psi}_{\bar{t}_-} + \psi \quad (16)$$

$$\omega_{\bar{t}_+} = \bar{\omega}_{\bar{t}_-} + \omega. \quad (17)$$

How much does E increase in time from adding a vortex at \bar{t} ? By using equations (16) and (17) in (9), we immediately obtain

$$E(\bar{t}_+) = E(\bar{t}_-) - \int \bar{\psi} \omega - \frac{1}{2} \int \psi \omega. \quad (18)$$

Since $\bar{\psi}$, ω and ψ are known explicitly, we can evaluate the right-hand side of (18) and thus update the energy. This new value of E defines the new state \bar{q} of the approximate solution via (15), with μ uniquely determined by E .

Pure decay

Let Δt denote the time interval between forcing by two successive random vortices. Given the approximate solution $\bar{\omega}$ at $t = \bar{t}_+$, we need to determine the evolution of the approximate dynamics during the decay phase, $\bar{t}_+ \leq t < \bar{t} + \Delta t$, up to the instant just before adding the next localized vortex, $t = \bar{t} + \Delta t$. To do so, we must determine the change in energy and circulation in a situation without forcing.

Since we do not have simple exact expressions that describe the evolution of E and Γ we need to estimate their change during decay. At the equilibrium statistical state defined by the closure algorithm at \bar{t}_+ , the nonlinear terms in (1) vanish identically. Thus, we approximate the evolution of q over $\bar{t}_+ \leq t < \bar{t} + \Delta t$ by

$$\frac{\partial q}{\partial t} = P_0(\Delta)\omega. \quad (19)$$

The solution reduces to the first-order Taylor approximation

$$\begin{aligned} \tilde{\omega} &= \bar{\omega} + (t - \bar{t})P_0(\Delta)\bar{\omega} \\ \tilde{\psi} &= \bar{\psi} + (t - \bar{t})P_0(\Delta)\bar{\psi}. \end{aligned} \quad (20)$$

To estimate the change in the energy, we remark that

$$\dot{E} = - \oint \psi \frac{\partial \omega}{\partial t}. \quad (21)$$

Since at $t = \bar{t}$ we have $\partial_t \omega = P_0(\Delta)\omega$, we approximate the change in energy over $(\bar{t}, \bar{t} + \Delta t)$ by

$$\dot{E}(t) = - \oint \tilde{\psi} P_0(\Delta)\tilde{\omega} + O((t - \bar{t})^2) \quad (22)$$

$$= - \oint [\bar{\psi} + (t - \bar{t})P_0(\Delta)\bar{\psi}] [P_0(\Delta)(\bar{\omega} + (t - \bar{t})P_0(\Delta)\bar{\omega})] + O((t - \bar{t})^2). \quad (23)$$

Integrating in time up to $t = t + \Delta t$ yields the following estimate for the change in the energy:

$$\begin{aligned} E(t + \Delta t) &= E(t) - \Delta t \oint \bar{\psi} P_0(\Delta)\bar{\omega} - \frac{1}{2}(\Delta t)^2 \oint [P_0(\Delta)\bar{\psi}][P_0(\Delta)\bar{\omega}] \\ &\quad - \frac{1}{2}(\Delta t)^2 \oint \bar{\psi}[P_0(\Delta)^2\bar{\omega}] - \frac{1}{3}(\Delta t)^3 \oint [P_0(\Delta)\bar{\psi}][P_0(\Delta)^2\bar{\omega}] + O(\Delta t^3). \end{aligned} \quad (24)$$

For the sake of clarity, we summarize the crude closure algorithm below.

Crude closure algorithm

0. At $t = 0$ match \bar{E} with the energy of the initial flow. This defines the initial approximate statistical state $\bar{q} = \bar{\omega} + h = \mu\bar{\psi}$.
1. Let \bar{E}_- denote the current approximate energy, which defines the statistical state $\bar{q} = \mu\bar{\psi}$ at $t = \bar{t}_-$. Compute the change in \bar{E} due to the addition of a localized vortex ω ,

$$\bar{E}_+ = \bar{E}_- - \oint \bar{\psi}\omega - \frac{1}{2} \oint \psi\omega. \quad (25)$$

This defines the new statistical state $\bar{\omega}$ at $t = \bar{t}_+$ via $\bar{q} = \mu\bar{\psi}$ with the energy \bar{E}_+ .

2. Compute the change in \bar{E} during decay, $\bar{t} < t < t + \Delta t$:

$$\begin{aligned}\bar{E}(t + \Delta t) = \bar{E}(t) - \Delta t \int \bar{\psi} P_0(\Delta) \bar{\omega} - \frac{1}{2}(\Delta t)^2 \int [P_0(\Delta) \bar{\psi}] [P_0(\Delta) \bar{\omega}] \\ - \frac{1}{2}(\Delta t)^2 \int \bar{\psi} [P_0(\Delta)^2 \bar{\omega}] - \frac{1}{3}(\Delta t)^3 \int [P_0(\Delta) \bar{\psi}] [P_0(\Delta)^2 \bar{\omega}].\end{aligned}\quad (26)$$

This defines the new statistical state \bar{q} at $t = \bar{t} + \Delta t$.

3. Return to 1.

We emphasize that the crude closure algorithm marches in time independently and without any knowledge of the solution of (1). It only requires the initial energy at $t = 0$, the applied external forcing and the values of the various dissipation coefficients.

2.2. Adding the circulation constraint

The crude closure algorithm presented in the previous section utilizes mean states, which are completely determined by the energy. A natural extension consists in including additional quantities from the infinite number of integrals conserved by the inviscid and unforced dynamics (12). This leads to a richer family of mean states and thus can possibly result in a crude closure, which adapts to a wider range of flow situations.

For example, the inclusion of the circulation constraint into the statistical theory yields the *linear* mean-field equation,

$$q^* = \mu \psi^* + \alpha. \quad (27)$$

Again μ and α are ratios of two Lagrange multipliers each; they are determined by the energy and the circulation. For each pair (μ, α) there is a unique solution to (27) for $\mu > -\lambda_1$, the smallest non-zero eigenvalue of the Laplacian in Ω . Thus we have obtained an augmented two-parameter family of statistical states. When the circulation constraint is absent, α vanishes and we recover the mean-field equation of the energy–enstrophy theory (15). Since the circulation of any flow in periodic geometry is identically zero, $\alpha = 0$ and the one- and two-parameter crude closure algorithms coincide in this special situation.

Next, we outline the modifications required to include the circulation into the crude closure algorithm from section 2.1. Let \bar{E} and $\bar{\Gamma}$ be the energy and circulation, which uniquely define the coarse-grained vorticity \bar{q} via (27). When a small random vortex ω is added to the flow at $t = \bar{t}$, the change in circulation is

$$\bar{\Gamma}(\bar{t}_+) = \bar{\Gamma}(\bar{t}_-) + \int \omega. \quad (28)$$

To estimate the change in circulation during pure decay, we use the first-order Taylor approximation (20), which yields

$$\bar{\Gamma}(t + \Delta t) = \bar{\Gamma}(t) + \Delta t \int P_0(\Delta) \bar{\omega} + \frac{1}{2} \Delta t^2 \int P_0(\Delta)^2 \bar{\omega}. \quad (29)$$

The update of the energy, \bar{E} , remains identical to that of the one-parameter crude closure described in section 2.1.

To conclude this section we briefly comment on implementation issues and, in particular, show an efficient method to determine α and μ from \bar{E} and $\bar{\Gamma}$. First, let

$$\psi^* = \psi_1 + \alpha \psi_2. \quad (30)$$

Hence ψ_1 and ψ_2 satisfy

$$\Delta\psi_1 + h = \mu\psi_1 \quad (31)$$

$$\Delta\psi_2 = \mu\psi_2 + 1 \quad (32)$$

where both ψ_1 and ψ_2 vanish on the boundary of Ω . We remark that the macrostates defined by (27) do not completely satisfy the ‘free-slip’ boundary conditions in (7) if Ω is the channel or the basin. Indeed, the free-slip boundary condition is satisfied by ψ_1 for all $p \geq 0$, but by ψ_2 only for $p = 0$. By adding higher-order derivatives on the right of (32) it may be possible to correct this slight inconsistency. Next for $\mu > -\lambda_1$, we compute and store the values of the energy, E_1 and E_2 , and of the circulation, Γ_1 and Γ_2 , for ψ_1 and ψ_2 , respectively. Hence the total energy and circulation are

$$\Gamma(\mu) = \Gamma_1(\mu) + \alpha\Gamma_2(\mu) \quad (33)$$

$$E(\mu) = E_1(\mu) + \alpha^2 E_2(\mu) - \alpha I(\mu) \quad I(\mu) = \oint \psi_1 \omega_2 \quad (34)$$

where we also store $I(\mu)$, which represents the interaction between ψ_1 and ψ_2 . Given $\bar{\Gamma}$ and \bar{E} we now match μ and α as follows. From (33) it follows that for any μ the corresponding value of α is

$$\alpha_\mu = \frac{\bar{\Gamma} - \Gamma_1(\mu)}{\Gamma_2(\mu)}. \quad (35)$$

By using that value for α in (34) we compute the corresponding energy throughout the entire range of μ . This cheap one-dimensional search then yields the desired μ at the value of $E(\mu)$ closest to \bar{E} .

Although we have implemented and tested crude closure dynamics based on the above two-parameter family of statistical states, we did not observe a significant improvement in accuracy. Indeed, in the majority of our numerical experiments, the results from the one-parameter crude closure are so accurate that the additional improvement provided by $\bar{\Gamma}$ is negligible. Furthermore, to accommodate the special flow configurations over layered topography presented in section 5, the mean-field equation must be nonlinear, unlike (27). Nevertheless, with the inclusion of the circulation constraint into the energy–enstrophy theory, the mean states can now represent flows with either positive or negative circulation. In contrast, the energy–enstrophy theory is unable to accommodate such a sign change and yields mean states whose relative vorticity is anticorrelated with the topography. As the energy increases and μ approaches $-\lambda_1$, the mean state is increasingly dominated by the contribution of the lowest Fourier mode of the topography. Hence if the lowest Fourier coefficient of h is positive, the mean statistical states of the energy–enstrophy theory in the basin geometry will tend to resemble a large vortex rotating clockwise as E increases. To demonstrate the greater versatility of two-parameter crude closure dynamics, we present in section 3.3 a situation of complete flow reversal, which cannot be predicted by the one-parameter crude closure algorithm.

2.3. More complex few-constraint statistical theories

The addition of the circulation constraint to the energy–enstrophy theory does not enrich sufficiently the family of statistical mean states to accommodate flow configurations such as those presented in section 5. However, the addition of a few judiciously chosen constraints from the infinite list in [12] might improve the performance of the crude closure algorithm significantly (see section 5). Following Turkington [12] and DiBattista *et al* [13], we utilize the extrema of the potential vorticity as additional conserved quantities besides the circulation

and the energy. Let Q_+ and Q_- denote the maximum and the minimum, respectively, of the initial potential vorticity field, where $Q = (Q_+ - Q_-)/2$ and $\bar{Q} = (Q_+ + Q_-)/2$ are the half-width and midpoint of the interval $[Q_-, Q_+]$, respectively. By repeating the calculations in [12, 13], the mean-field equation in this setting becomes

$$q^* = \bar{Q} + Q\mathcal{L}[Q(\theta\psi^* - \gamma)] \quad \text{where } \mathcal{L}[z] = \coth z - \frac{1}{z} \quad (36)$$

is the classical Langevin function. Again θ and γ are Lagrange multipliers associated with the energy and the circulation constraints. In contrast to the mean-field equation in (27), the mean-field equation in (36) is *nonlinear*. It involves two additional parameters, Q_+ and Q_- , and therefore yields a richer family of statistical states. To compute the entropy maximizing probability distribution, ρ^* , for given E_0 , Γ_0 , Q_+ and Q_- , we use the algorithm developed by Turkington and Whitaker [23]. This approach is based on the Kuhn–Tucker formulation of the above constrained optimization problem and proceeds by successive linearization of the energy constraint. DiBattista *et al* [13] extended this procedure to a non-zero mean flow with a beta effect and explored flow configurations spanned by the entire parameter space. In particular, they identified the parameter regimes for which the entropy maximizing flow in a channel without topography bifurcates from a ubiquitous shear flow to a monopolar vortex. In section 5 we trivially modify this algorithm for flow over topography and determine the mean-field potential vorticity, q^* , defined by the entropy maximizer ρ^* .

2.4. Diagnostics

We shall compare the ‘exact’ (numerical) solution with two types of approximate statistical states. On that hand, we shall verify the *consistency* of the equilibrium statistical theories in a non-equilibrium regime simply by matching the instantaneous exact energy E of the flow. Thus, given the exact computed value of E , we compare the statistical state $q^* = \mu^*\psi^*$ with the exact solution q , where μ^* is determined by E . On the other hand, we shall measure the *accuracy* of the crude dynamic closure by comparing the approximate statistical state \bar{q} , defined above by the crude dynamics algorithm, with the exact solution q . Although one might initially be led to believe that the macrostates obtained by matching E to those of the exact solution would give much better results, we will provide ample numerical evidence that this is not so. On the contrary, because the evolution of bulk features in the flow, such as the energy, will prove to be remarkably well predicted, even under the harshest conditions, by the crude closure algorithm, both error measures based either on accuracy or on consistency tend to agree extremely well; in fact, it is usually quite difficult to distinguish between them in any given situation.

To verify the consistency of the equilibrium statistical theory, we need to compare in a quantitative fashion how close the instantaneous vorticity q and its corresponding stream function ψ come to satisfying (13). We introduce the correlation function of f and g

$$\text{Corr}(f, g) = 1 - \frac{(f, g)^2}{\|f\|^2 \|g\|^2} \quad (37)$$

where (f, g) denotes the L_2 -inner product on Ω and $\|f\|_2$ its corresponding L_2 -norm. We recall that the correlation satisfies $0 \leq \text{Corr}(f, g) \leq 1$ and that the correlation is zero if and only if f and g are collinear, that is

$$\text{Corr}(f, g) = 0 \iff f(x, y) = c g(x, y) \quad \text{for some constant } c \neq 0. \quad (38)$$

Thus we calculate $\text{Corr}(q, \psi)$ to measure how well q satisfies (13).

To calculate the accuracy of the crude closure algorithm, we must compare the exact solution q either with the macrostate q^* , where E is simply matched to the exact solution, or with the statistical state \bar{q} , which is also defined by (13) but with \bar{E} predicted by the crude closure algorithm described above. We shall use two different error measures, the relative L_2 -error in the vorticity,

$$\text{Err}(q, q^*) = \frac{\|q(t, \cdot) - q^*(t, \cdot)\|_2}{\|q(t, \cdot)\|_2} \quad (39)$$

and the relative L_2 -error in the velocity,

$$\text{Err}(\vec{v}, \vec{v}^*) = \frac{\|\vec{v}(t, \cdot) - \vec{v}^*(t, \cdot)\|_2}{\|\vec{v}(t, \cdot)\|_2}. \quad (40)$$

Both error measures quantify the relative closeness of either statistical state, \bar{q} or q^* , to the exact solution, q . Since we are strongly perturbing the flow with random localized vortices, we expect larger errors in the vorticity. Indeed, equation (39) is a very tough measure of the relative closeness between two solutions of (1) with random forcing; in particular, when $v = 0$ there is no inherent dissipative mechanism but hyperviscosity to remove small scales in the flow.

The following two diagnostic quantities, both enstrophy–energy ratios, will prove useful in assessing the range of validity of the crude closure:

$$\Lambda_\omega(t) = \frac{\int \omega^2}{\int |\nabla \psi|^2} \quad (41)$$

$$\Lambda_q(t) = \frac{\int q^2}{\int |\nabla \psi|^2}. \quad (42)$$

Note that both Λ_ω and Λ_q have the units $(\text{length})^{-2}$ and hence their square roots provide indicators of an average inverse length scale. We use Λ_ω , the second moment of the energy spectrum, as a measure of the roughness of the flow, whereas the magnitude of Λ_q will prove a clear indicator for the performance of the crude closure, with improved performance at lower values. Although strongly perturbed flows often produce large relative errors in velocity, the crude closure algorithm is usually able to track the evolution of bulk features of the flow quite accurately, as long as Λ_q is not too big. Large values of Λ_q indicate that most of the energy in the flow cannot reside in large-scale coherent structures.

The large-scale Reynolds number, Re , is defined as

$$Re = \frac{L |\vec{v}|_{\max}}{v} \quad (43)$$

where $L = 2\pi$ for the torus or the channel and $L = \pi$ for the basin.

2.5. Numerical method

We solve the barotropic flow equations (1) numerically on a 2π -periodic domain with a pseudo-spectral method. Thus we compute the spatial derivatives $\vec{v} = \nabla^\perp \psi$ and $\nabla \vec{q}$ in Fourier space, but then evaluate the product $\vec{v} \cdot \nabla \vec{q}$ in physical space. The numerical scheme proceeds in time by using a split-step procedure, where the diffusive part is handled exactly in Fourier space. The nonlinear convective part is computed with an explicit fourth-order Runge–Kutta method with adaptive time stepping, to ensure stability as the flow accelerates. As the flow decelerates, however, we keep the time step δt at least 10 times smaller than the time interval Δt between two subsequent localized vortices. For simplicity, we set the time step in the

Taylor approximation equal to the time step of the Runge–Kutta scheme. The value of the hyperviscosity, $\nu_H = 10^{-7}$, was found to guarantee numerical stability and effectively remove unresolved features on the 128×128 grid, which we used in all our calculations.

While we cannot claim that there is detailed numerical resolution for the smallest vortices in the computations, their effect on the large-scale features of the flow nevertheless is negligible for the computations presented here. Comparisons of numerical solutions on different grids showed that bulk features of the flow, such as the energy or the L_2 -error in velocity, hardly change if we further refine the underlying grid (see also [15]).

Random forcing

The evolution of the dynamics is governed by the external forcing F and is chosen to mimic a random bombardment of the flow with smoothed small-scale vortices,

$$F(x, y, t) = \sum_{j=1}^{\infty} \delta(t - t_j) \omega_r(\vec{x} - \vec{x}_j). \quad (44)$$

The smoothed small-scale vortex is added at the random location \vec{x}_j and has support in a disc of radius r_j ,

$$\begin{aligned} \omega_r(\vec{x}) &= A \left(1 - \frac{|\vec{x} - \vec{x}_j|^2}{r_j^2} \right)^2 & |\vec{x} - \vec{x}_j| \leq r_j \\ \omega_r(\vec{x}) &= 0 & |\vec{x} - \vec{x}_j| > r_j. \end{aligned} \quad (45)$$

The random locations \vec{x}_j are uniformly distributed inside Ω within a narrow margin away from the boundary of Ω . The radii r_j of the vortex patches vary randomly between $4\Delta x$ and $8\Delta x$, where $\Delta x = 2\pi/128$ is the mesh size. We approximate the temporal delta functions in (44) by the large constant value $1/\delta t$ over the time interval, $t_j \leq t \leq t_j + \delta t$, where δt is the current step size. In all calculations the amplitude $|A|$ of the added vortices remained constant for all time, yet we allow for a sign change of A . The value of A is either equal to one or to a percentage of the maximal vorticity of the initial flow configuration. Unless the forcing is identically zero, the time interval between two subsequent vortices remained constant and equal to $\Delta t = 0.1$ in all computations. Thus, during a numerical experiment up to $t = 1000$, the flow has been bombarded with 10 000 smoothed point vortices, while the numerical integration has performed at least 100 000 time steps. The required increasingly smaller time steps at higher velocities remain the major obstacle to long-time numerical experiments at higher Reynolds numbers. In contrast, the crude closure algorithm is not affected by the Reynolds number; in fact, it tends to perform better at higher Reynolds number.

Random topography

In sections 3 and 4 we shall use the random topography,

$$h(x, y) = H \sum_{1 \leq |\vec{k}| \leq 5} h_{\vec{k}} e^{i\vec{k} \cdot \vec{x}} \quad \vec{x} = (x, y) \quad \vec{k} = (k_1, k_2) \quad (46)$$

where

$$h_{\vec{k}} = \frac{H_0}{|\vec{k}|^2} e^{i\theta_{\vec{k}}} \quad h_{-\vec{k}} = h_{\vec{k}}^*. \quad (47)$$

Here the constant H_0 normalizes the coefficients $h_{\vec{k}}$ to ensure that the maximal total height is H , and the random phase shifts $\theta_{\vec{k}}$ are chosen from a uniform distribution in $[0, 2\pi)$. Due to

the decay of the Fourier coefficients like $|\vec{k}|^{-2}$, the topography is smooth. A medium-sized topography corresponds to $H = 1$, whereas $H = 10$ corresponds to a rather tall topography. For random topography in the channel or basin, we impose the appropriate symmetry condition in (46) to ensure that $h(x, y)$ vanishes on the boundary of Ω . The random layered topography in section 5 is obtained through a one-dimensional expansion in sine functions analogous to (46).

3. Topographic flows in a basin

We shall now submit the crude closure dynamics presented in section 2 for barotropic flow over topography to a series of successively more stringent tests. The underlying random topography is chosen according to (46) with $H = 1$; it is shown in figure 1 and respects the symmetry imposed by the basin geometry. The contours of topographic height are shown in the top left-hand frames of figures 4 and 6 (in figure 4 a small initial vortex added *ab initio* is clearly visible against the contours of h).

3.1. Decaying flow

We begin with a purely decaying flow situation and thus set $F = 0$ in (1). The initial flow configuration is set to a perturbed steady state with $\mu = -1.5$. The perturbation consists

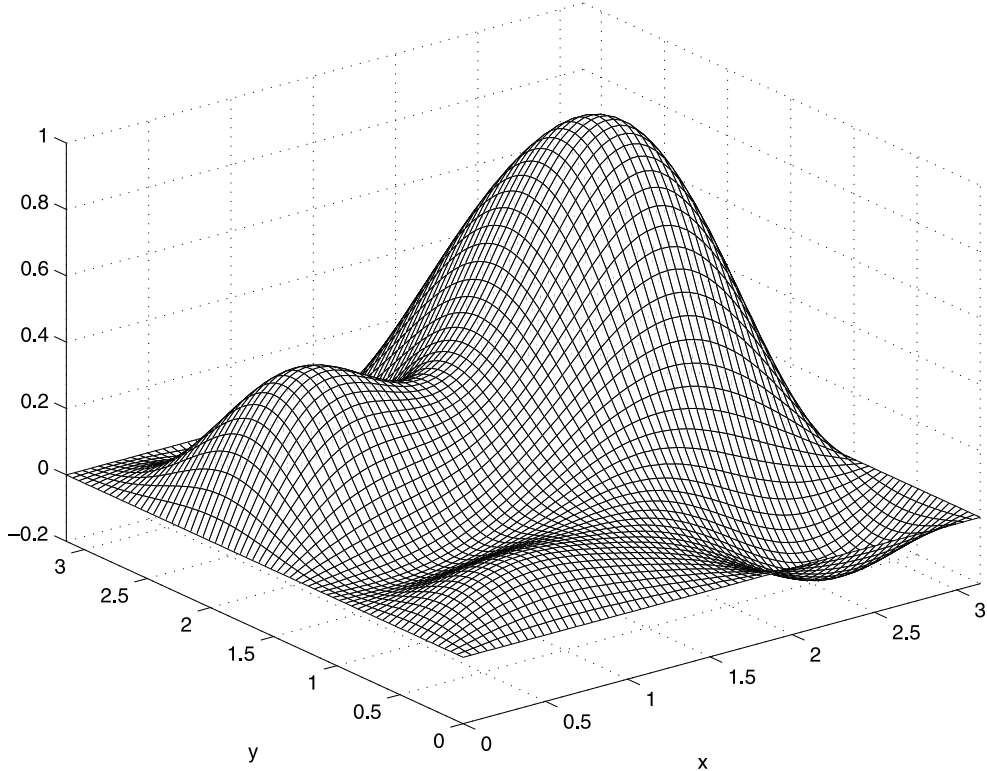


Figure 1. Random topography in the basin. The contours of topographic height are shown in the top left-hand frames of figures 4 and 6.

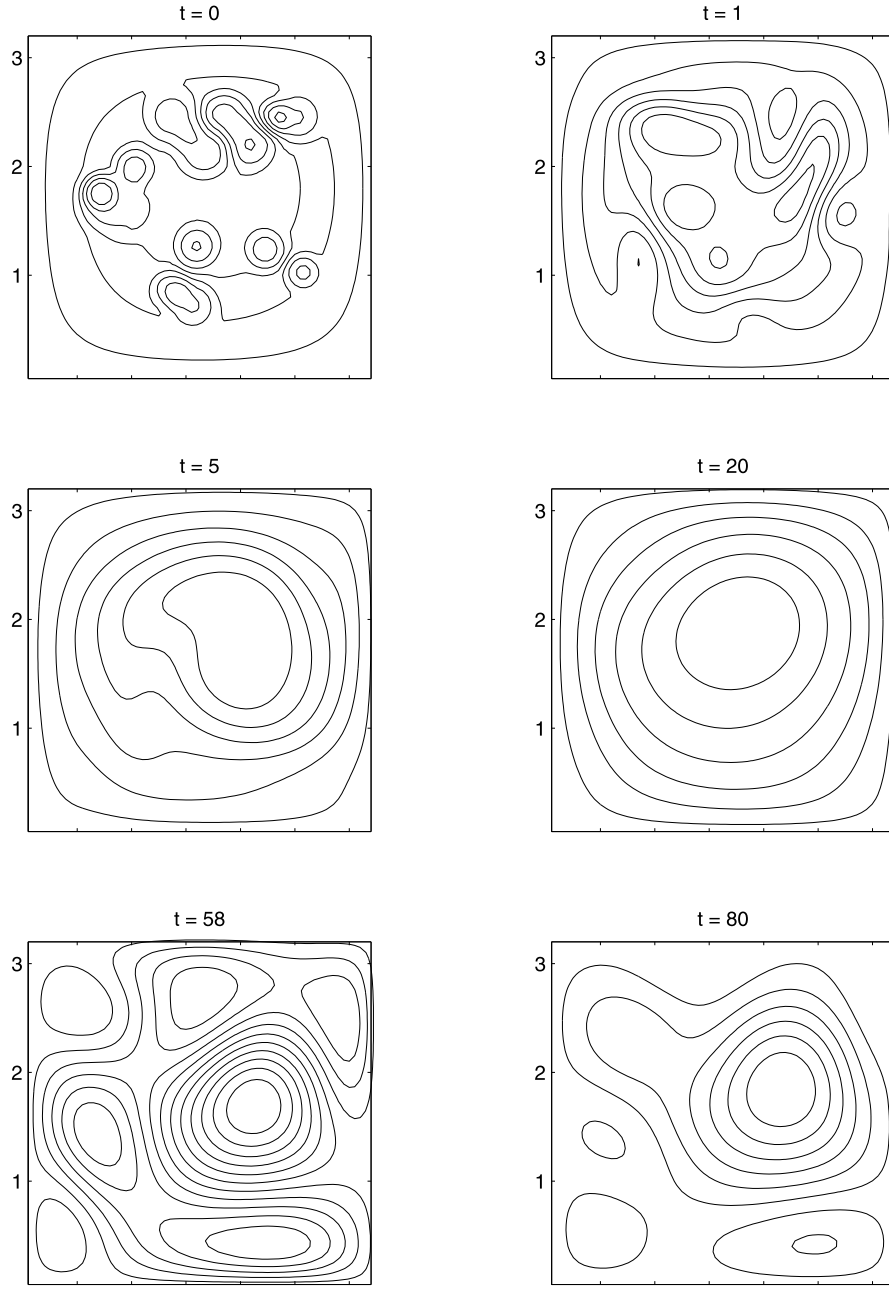


Figure 2. Snapshots of the potential vorticity at $t = 0, 1, 5, 30, 58, 80$ during pure decay in the basin, with $H = 1$ and $\nu = 0.01$.

of 16 random vortices, eight rotating clockwise and eight rotating counterclockwise, with fixed amplitude equal to 50% of the maximal initial vorticity, $|\omega|_{\max} \simeq 3.5$. The Ekman drag coefficient is set to $d = 0$ and the viscosity to $\nu = 0.01$, which results in a Reynolds number $Re = 400$. Figure 2 depicts selected snapshots of the potential vorticity at times

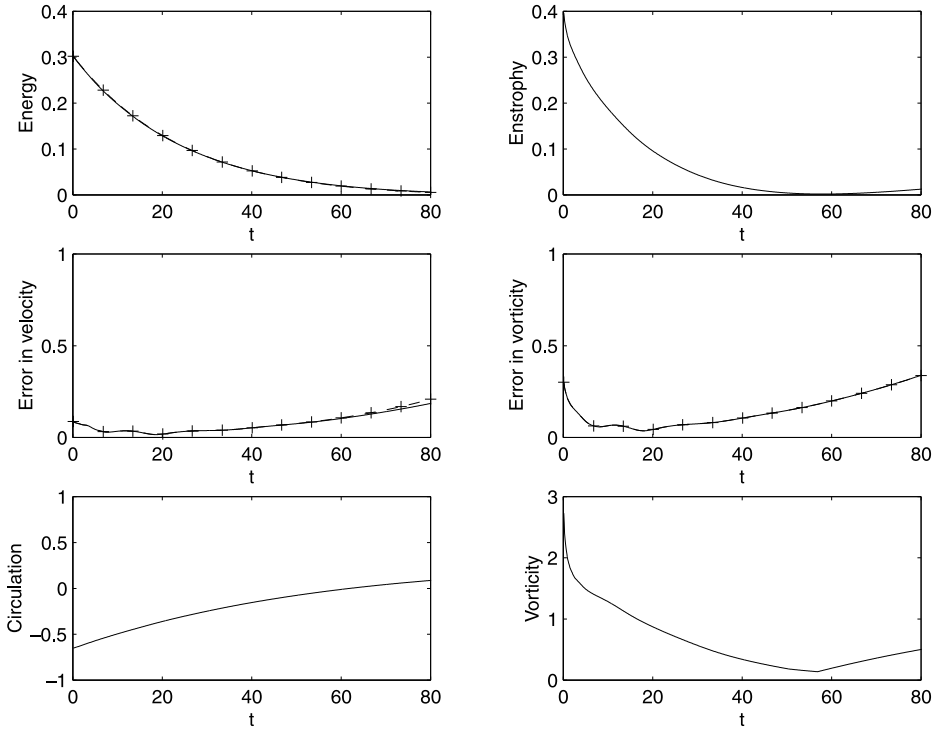


Figure 3. Comparison with crude closure dynamics during pure decay in the basin, with $H = 1$ and $v = 0.01$. Top left, energy E (—) and predicted energy \bar{E} (+); top right, enstrophy \mathcal{E} ; middle left, relative errors in matched velocity $\text{Err}(\vec{v}, \vec{v}^*)$ (—) and predicted velocity $\text{Err}(\vec{v}, \bar{\vec{v}})$ (+); middle right, relative errors in matched potential vorticity $\text{Err}(q, q^*)$ (—) and predicted potential vorticity $\text{Err}(q, \bar{q})$ (+); bottom left, circulation Γ ; bottom right, potential vorticity q .

$t = 0, 1, 5, 20, 58, 80$. The small-scale vortices, entrained by the background flow, interact and merge rapidly to form a large vortex, which spreads to the boundary of the domain. These initial stages clearly parallel the long-time behaviour of solutions to the two-dimensional (2D) Navier–Stokes equations (without topography) predicted by the theory of selective decay (see Majda and Holen [14]). Yet, as the flow evolves further in time, small vortex structures begin to emerge and eventually correlate with the topography.

Figure 3 provides the explanation to this peculiar long-time behaviour of the flow. During the initial phase of decay the energy, the enstrophy and the maximal potential vorticity consistently decrease with time while the circulation clearly remains negative. The evolution of the flow is dictated by the relative vorticity, ω , which dominates the potential vorticity $q = \omega + h$. Here topography plays a minor role and the flow evolution bears a resemblance to the Taylor vortex predicted by selective decay for flow without topography [14]. However, as the relative vorticity decreases further, the circulation changes sign, while both \mathcal{E} and $|q|_{\max}$ begin to increase again. During this second phase of pure decay the topography dominates the dynamics of the potential vorticity. Eventually ω approaches zero which results in the strong correlation of q and h . This numerical solution exhibits some of the behaviour noted in the classical study from [19].

In figure 3 we compare the exact (numerical) solution with the approximate solutions defined by the statistical states. The middle two frames show the relative errors in the

macrostates q^* , obtained by matching the value of the energy from the exact solution. Both the relative errors in \vec{v} and in q lie below 10% until $t = 50$. At later times the relative errors increase but this is somewhat misleading since these flows have nearly zero energy. As expected, the relative error in q is larger than the relative error in \vec{v} .

Next, we study the accuracy of the approximate solution \bar{q} determined by the crude closure algorithm. In the upper left-hand frame of figure 3, the exact energy, E , and the approximate energy, \bar{E} , are shown. The two curves can barely be distinguished from each other, which demonstrates that the crude closure predicts the evolution of the energy remarkably well. We recall that the crude closure dynamics evolves independently and without knowledge of the numerical solution, once the energy of the initial state has been matched at $t = 0$. Since the statistical states are completely determined by \bar{E} , which essentially coincides with the exact energy E , the relative L_2 -errors of the macrostates obtained via the crude closure dynamics also coincide with those obtained through direct matching. Hence, the resolved flow from the numerical solution provides little extra information for bulk features of the flow compared with the crude closure algorithm.

3.2. Spin-up of a large vortex

Here we consider a numerical experiment which is radically different from the previous one. Initially at rest, the flow is bombarded with localized vortices of like negative sign and constant amplitude $|A| = 1$. What is the statistical quasi-equilibrium state for large times with damping and driving?

In our first calculation we set $\nu = 0.01$, so that statistical equilibrium was reached around $t \simeq 500$, with a final Reynolds number close to 2200. Since the macrostates are not defined for zero energy ($E \rightarrow 0$ implies $\mu \rightarrow \infty$), we add a single random vortex to the quiescent flow and use the corresponding energy to initialize the crude closure algorithm. Then the initial energy at $t = 0$ is small but positive, typically $E(0) = O(10^{-4})$.

Figure 4 depicts snapshots of the potential vorticity during initial and later stages in the computation, $t = 0, 1, 5, 10, 50, 2000$. At $t = 0$ the small vortex added *ab initio* is clearly visible against the contour lines of the topography. The initial stages of the flow are strongly perturbed and incoherent, yet with time a vortical super-structure emerges from the turbulent flow with the vorticity concentrated in the centre of the basin. In figure 5 we see the large increase in energy, as the flow accelerates due to the incessant bombardment with small vortices up to $t = 2000$ —until that time 20 000 random vortices have been added. The circulation, negative since the flow rotates clockwise, decreases below -5 . The two middle frames in figure 5 display the errors in velocity and vorticity using the macrostates obtained by matching the energy of the exact solution. The relative errors, as expected, are quite large during the initial stages, but rapidly decrease and reach remarkably small values considering the crude closure being utilized: 2% for the velocity and 5% for the vorticity. Simultaneously, the correlation is very poor during initial stages but drops down significantly to values around 0.002 for larger time, while Λ_ω and Λ_q stabilize about moderate values, indicative of prevailing large-scale structures and smooth flow features. The lower two frames of figure 5, which focus on the initial stages of the flow, emphasize the incoherent initial flow stages governed by a rough small-scale interaction with poor correlation and high values of Λ_ω and Λ_q . Both Λ_ω and Λ_q rapidly reach values close to $\lambda_1 = 2$.

At this stage we address a remaining crucial issue: is the crude closure dynamics able to bridge over the initial chaotic stages of the flow and predict the bulk features of the emerging super-vortex? Surprisingly, the answer to this question is yes. Indeed, in the middle two frames

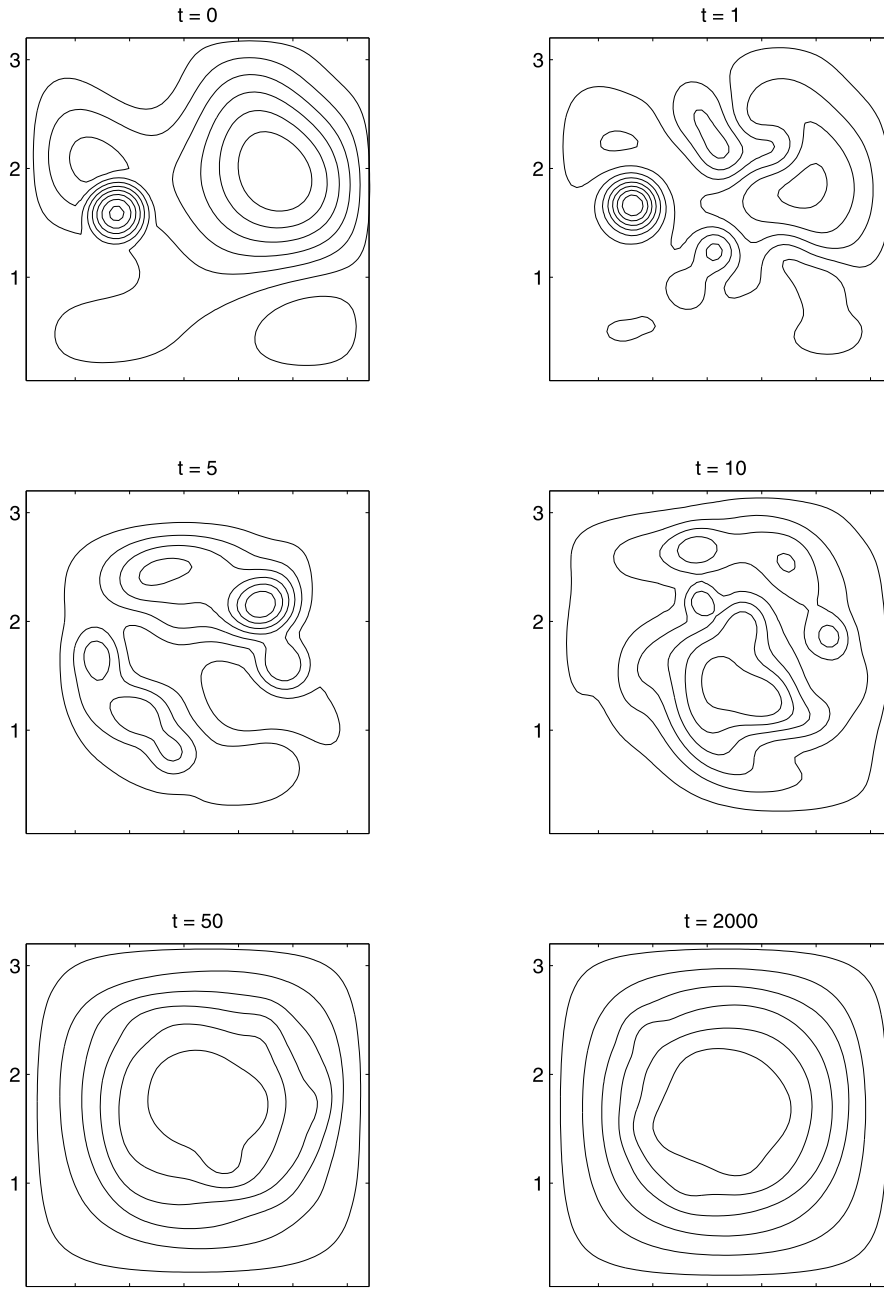


Figure 4. Snapshots of the potential vorticity at $t = 0, 1, 5, 10, 50, 2000$, during spin-up from zero in the basin, with $H = 1$ and $\nu = 0.01$.

in figure 5, the errors in velocity and vorticity obtained with the crude closure algorithm are barely larger than those obtained by the simple matching procedure.

How much do the results depend on the size of the topography? To answer this question we magnify the topography by a factor of ten and repeat the previous numerical experiment, with

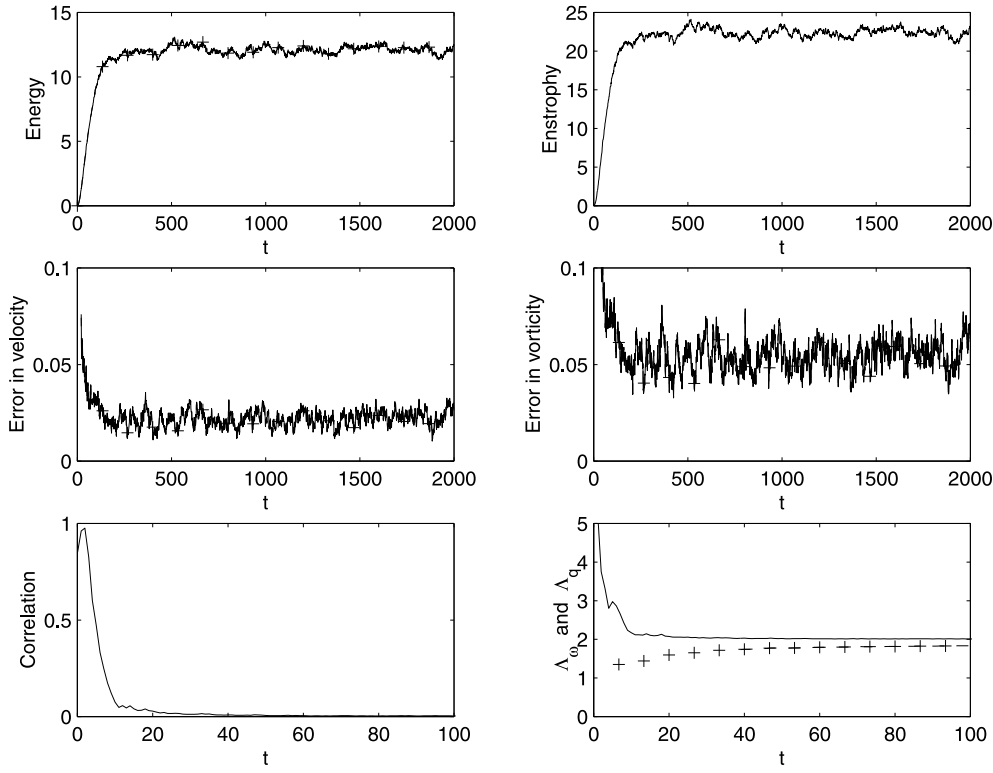


Figure 5. Comparison with crude closure dynamics during spin-up from zero in the basin, with $H = 1$ and $\nu = 0.01$. Top left, energy E (—) and predicted energy \bar{E} (+); top right, enstrophy \mathcal{E} ; middle left, relative errors in matched velocity $\text{Err}(\vec{v}, \vec{v}^*)$ (—) and predicted velocity $\text{Err}(\vec{v}, \bar{\vec{v}})$ (+); middle right, relative errors in matched potential vorticity $\text{Err}(q, q^*)$ (—) and predicted potential vorticity $\text{Err}(q, \bar{q})$ (+); bottom left, correlation $\text{Corr}(q, \psi)$; bottom right, Δ_ω (—) and Δ_q (+).

$H = 10$ in (46). Again, under the constant bombardment with random like-signed vortices, the flow undergoes a transient incoherent state masked by the dominating topography, while q remains strongly correlated to h . However, as the flow picks up speed and ω decreases further, the enstrophy reaches zero by $t = 38$ and the correlation of q and ψ becomes very poor. At this stage, topography and relative vorticity compete until the potential vorticity rearranges itself and a large vortex emerges to fill the basin (see figure 6). Beyond the initial perturbed flow configurations, the flow correlates extremely well with the statistical states. In the middle two frames of figure 7, we see the remarkable performance of the crude closure algorithm, with relative errors again about 2% for the velocity and 5% for the vorticity. Until $t = 100$ the relative errors in velocity of the macrostates obtained by matching the exact energy lie slightly below those predicted by the crude closure; however, at later times the crude closure recovers the same level of accuracy. We refrain from showing long-time simulations as the significant differences from the previous case with smaller topography occur only during the initial stages of the simulation.

The wide range of possible parameter settings is well represented by the above two situations of medium-sized and tall topography. If one increases the topography even further without increasing the forcing, the flow eventually lingers in a low-energy state governed by

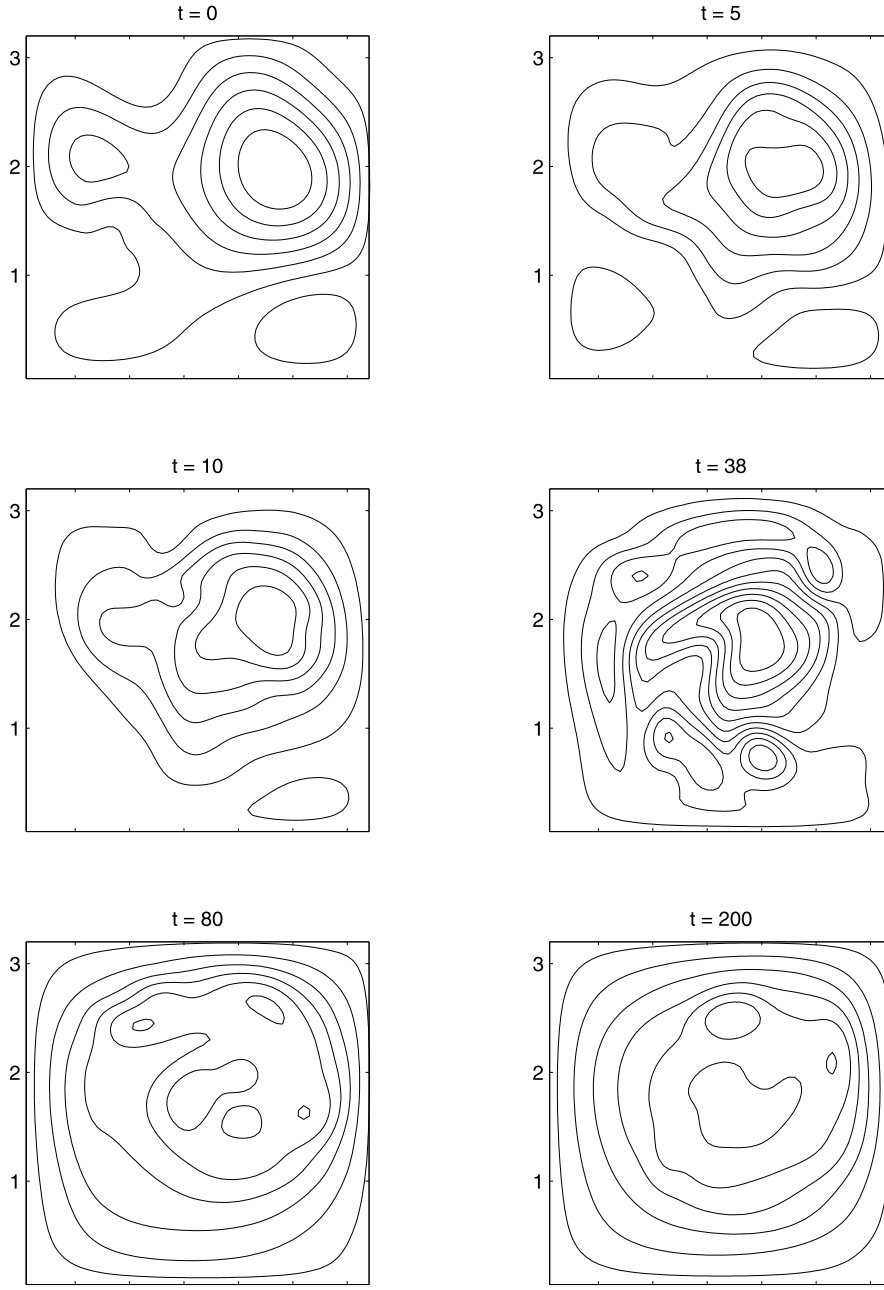


Figure 6. Snapshots of the potential vorticity at $t = 0, 5, 10, 38, 80, 200$, during spin-up from zero in the basin, with $H = 10$ and $\nu = 0.01$.

the underlying topography. Consequently, the value of Λ_q remains large and the performance of the crude closure is poor due to the small amount of mixing. In contrast, smaller topography leads to behaviour which is increasingly similar to that without topography, where the crude closure performs well (see [15]). Higher Reynolds number flows yield similar results but the

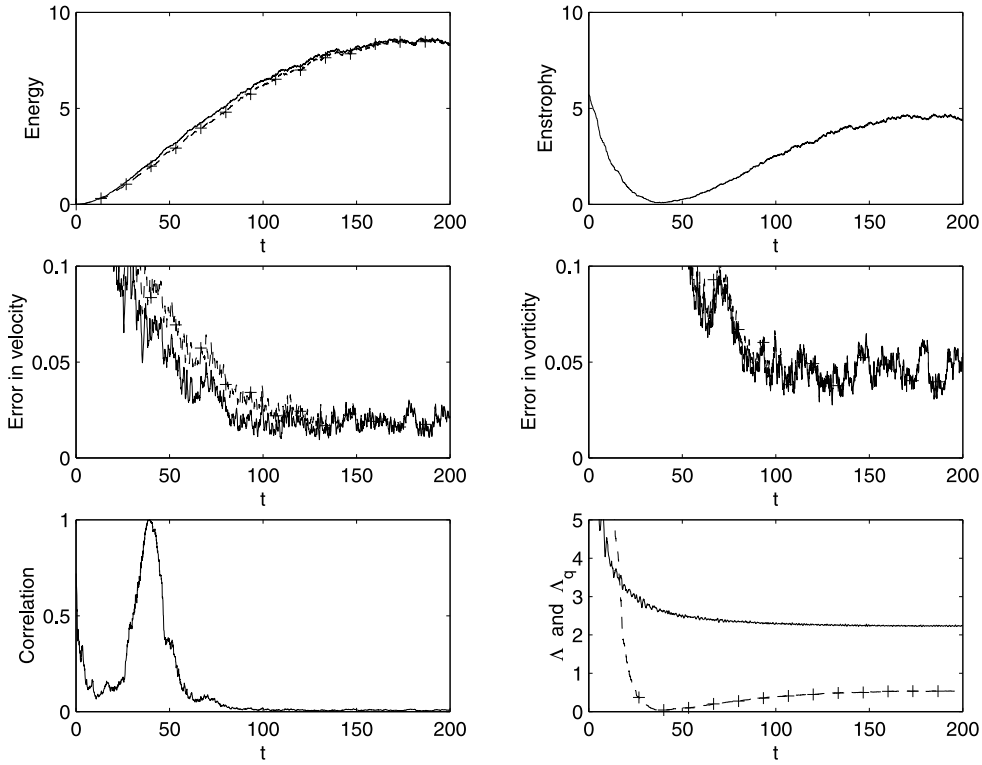


Figure 7. Comparison with crude closure dynamics during spin-up from zero in the basin, with $H = 10$ and $\nu = 0.01$. Top left, energy E (—) and predicted energy \bar{E} (+); top right, enstrophy \mathcal{E} ; middle left, relative errors in matched velocity $\text{Err}(\vec{v}, \vec{v}^*)$ (—) and predicted velocity $\text{Err}(\bar{\vec{v}}, \bar{\vec{v}})$ (+); middle right, relative errors in matched potential vorticity $\text{Err}(q, q^*)$ (—) and predicted potential vorticity $\text{Err}(\bar{q}, \bar{q})$ (+); bottom left, correlation $\text{Corr}(q, \psi)$; bottom right, Λ_ω (—) and Λ_q (+).

flows do not reach statistical equilibrium until much later times. We omit showing results with combined Newtonian viscosity and Ekman drag, as they are quite similar.

3.3. Flow reversal

Here we consider a numerical experiment which demonstrates the higher versatility of the crude closure dynamics based on the two-parameter family of statistical states defined by (27). As previously mentioned (see section 2.2), the energy–enstrophy theory is limited to mean statistical states where the relative vorticity and the topography are anticorrelated. For the random topography shown in figure 1, the mean state of the energy–enstrophy theory always resembles a large vortex rotating clockwise (negative vorticity) as the energy increases and μ approaches $-\lambda_1$. For instance, the top left-hand frame in figure 8 shows the mean state defined by (15) with $\mu = -1.5$. What if we bombard such a mean state with small-scale smoothed vortices of like positive sign and constant amplitude $|A| = 1$? The large vortex structure, initially rotating clockwise, begins to disintegrate and is completely destroyed by $t = 4$, as shown in figure 8. Under the incessant action of the external forcing, the flow lingers in an incoherent intermediate state, reverses its direction, and starts to rebuild a vortical structure with opposite sign. In addition to Newtonian dissipation, $\nu = 0.01$, we have included here

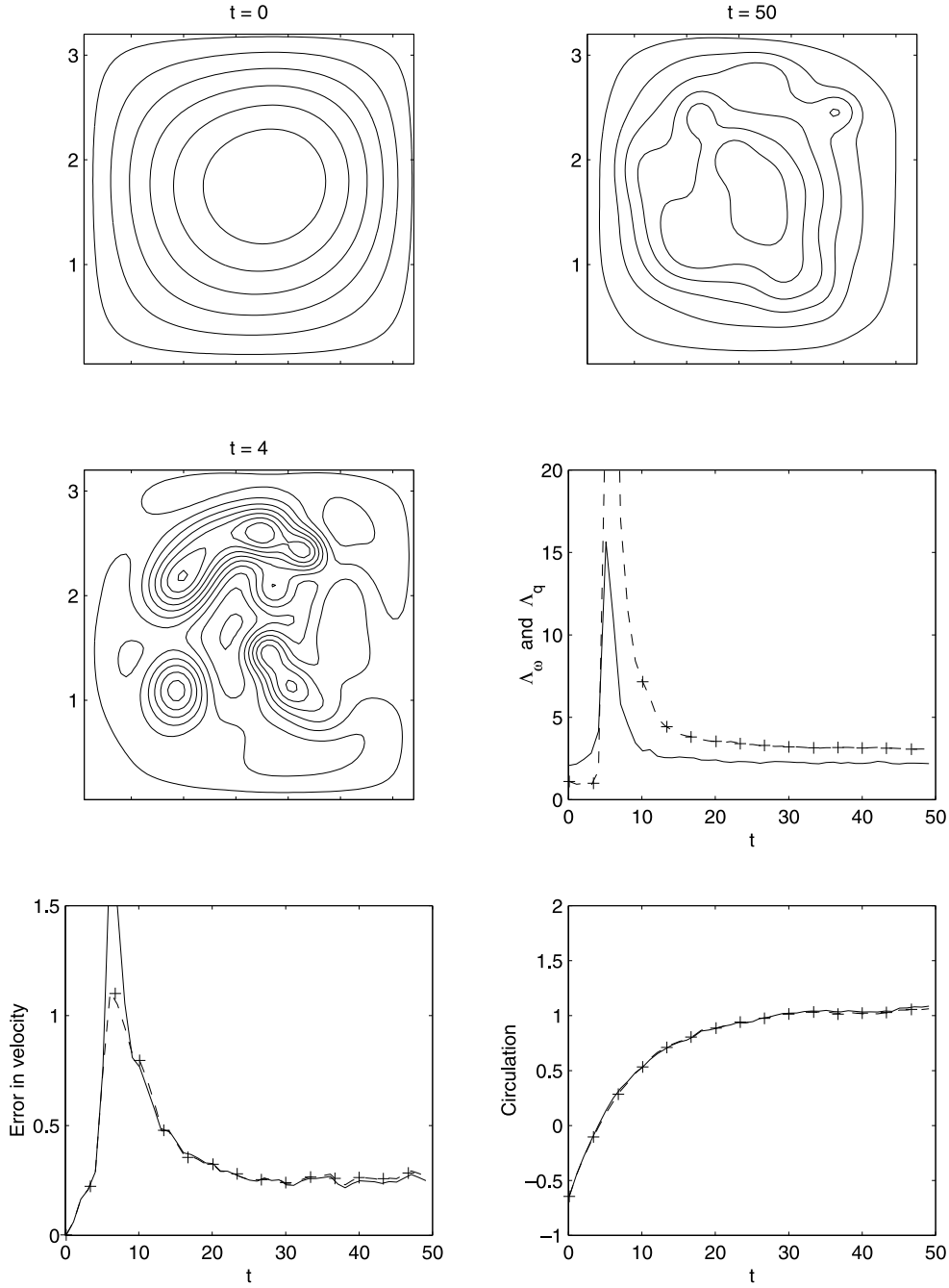


Figure 8. Comparison with two-parameter crude closure dynamics during flow reversal in the basin, with $H = 0.1$, $d = 0.1$ and $\nu = 0.01$. Top, snapshots of potential vorticity at $t = 0$ (clockwise flow) and $t = 50$ (counterclockwise flow); middle left, potential vorticity at $t = 4$; middle right, Λ_ω (—) and Λ_q (+); bottom left, relative errors in matched velocity $\text{Err}(\vec{v}, \vec{v}^*)$ (—) and predicted velocity $\text{Err}(\vec{v}, \tilde{\vec{v}})$ (+); bottom right, circulation Γ (—) and predicted circulation $\bar{\Gamma}$ (+).

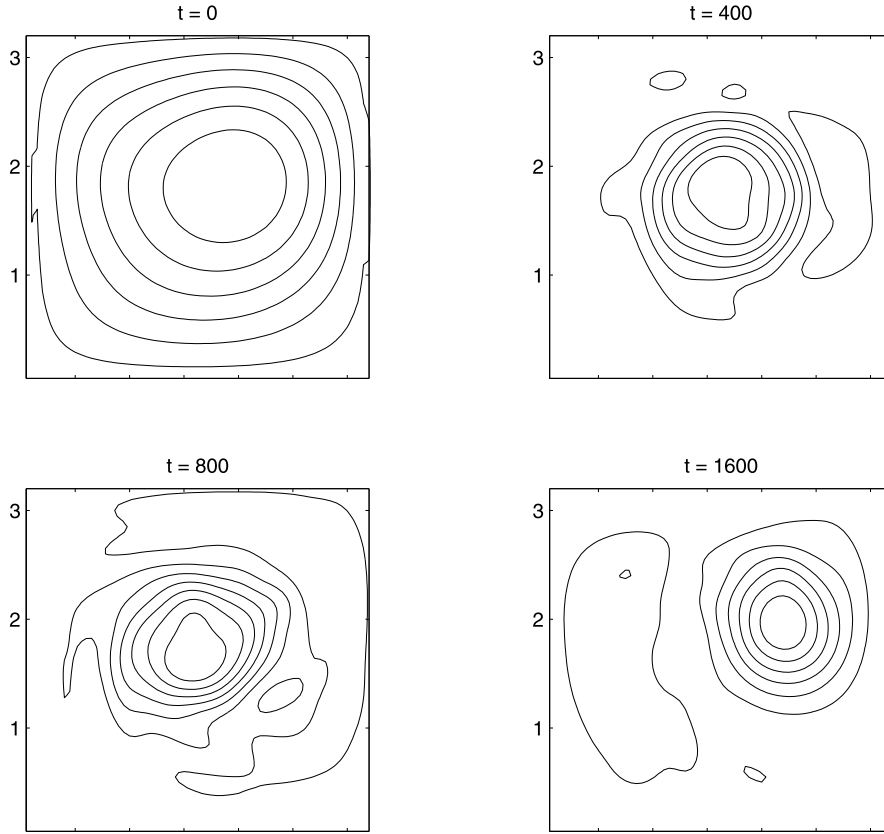


Figure 9. Snapshots of the potential vorticity at $t = 0, 400, 800, 1600$, in the basin during bombardment with localized vortices of alternating sign and amplitude equal to 10% of the initial maximal vorticity.

Ekman drag, $d = 0.1$, so that the flow rapidly reaches its new quasi-equilibrium state at a similar energy level, $E \simeq 0.3$. As the energy–enstrophy theory cannot accommodate such a sign change, the one-parameter crude closure algorithm fails to predict the flow behaviour past the incoherent stages. With the inclusion of the circulation constraint, the mean statistical states defined by (27) can account for such a sign change in vorticity. During the transient incoherent stages the relative errors in velocity reach values beyond 100%, while the large values of Λ_ω and Λ_q indicate the dominance of smaller scales. However, once past the transient stages, the relative errors in velocity decrease again and the two-parameter crude closure predicts the emergence of a large-scale vortex with opposite sign. The approximate circulation, $\bar{\Gamma}$, predicted by the crude closure dynamics according to (28) and (29), follows closely the evolution of Γ , as shown in figure 8.

3.4. Forcing by alternating opposite-signed vortices

Finally, we attempt to explore the limits of the statistical theory and set $\nu = 0$. The hyperviscosity remains active with $\nu_H = 10^{-7}$. By strongly perturbing the flow with random localized vortices of alternating opposite sign, we attempt to force it out of the statistical state and test the performance of the crude closure algorithm. Figure 9 displays snapshots of the

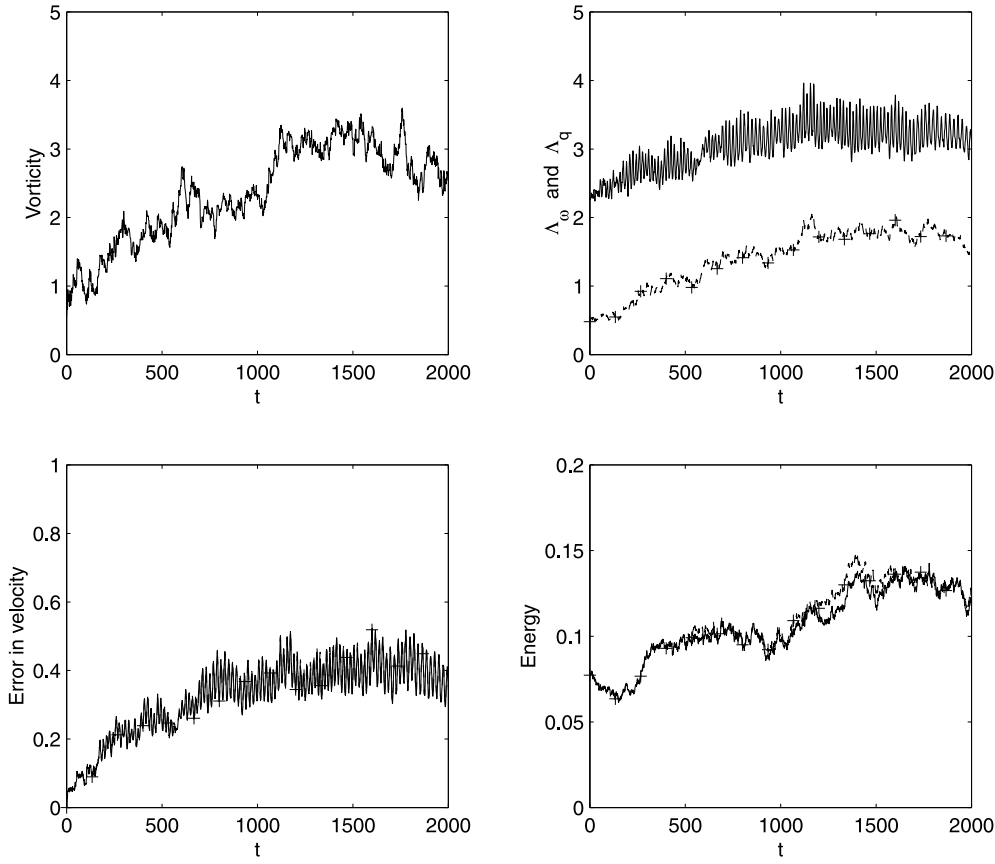


Figure 10. Comparison with crude closure dynamics during bombardment with localized vortices of alternating sign and amplitude equal to 10% of initial maximal vorticity. Top left, maximal potential vorticity $|q|_{\max}$; top right, Λ_ω (—) and Λ_q (+); bottom left, relative errors in matched velocity $\text{Err}(\vec{v}, \vec{v}^*)$ (—) and predicted velocity $\text{Err}(\vec{v}, \tilde{\vec{v}})$ (+); bottom right, energy E (—) and predicted energy \tilde{E} (+).

potential vorticity at times $t = 0, 400, 800, 1600$. The initial flow configuration corresponds to the steady state with $\mu = -1$. Since the initial energy is not zero in this case, the crude closure is well defined from the start and no small vortex needs to be added at $t = 0$. In contrast to the behaviour during pure decay or build-up from zero, the contour lines of the potential vorticity rapidly concentrate in the centre of Ω . Then, by $t = 800$, a large secondary vortex structure appears along the boundary of Ω as the main vortex shifts away from the centre and wanders about the basin. As to be expected under such harsh conditions, the statistical states correlate rather poorly with the evolving flow and lead to errors of around 40% in the velocity. In figure 10 the strong variations in the maximal velocity and the constant increase of both Λ_ω and Λ_q indicate the increasingly strong activity on small scales. Surprisingly, the crude closure is able to track bulk features of the flow, such as the energy, quite accurately and for all time, in spite of poor correlation and large relative errors in the velocity. Note that the evolution of the energy predicted by the crude closure departs only slightly from that of the exact energy around $t = 1200$ and that the two curves meet again around $t = 1500$. Although increasing ν always leads to smoother flows and smaller relative errors, the net input of energy

of the alternating small-scale forcing remains marginal and as a consequence the flow rapidly decays to zero.

4. Topographic flows in a channel

With the clear evidence presented in the previous section for the merit of the crude closure dynamics in damped and driven flows in a basin, it is natural to ask whether similar behaviour can be expected in a different geometry. In this section we choose Ω to be a channel and set h again to be a random topography with $H = 1$, sampled according to the prescription in (46) and shown in figure 11. The contours of topographic height are shown in the top left-hand frame of figure 12, where a small initial vortex added *ab initio* is clearly visible against the contours of h . We remark that due to our initial assumption that ψ and h vanish on the boundary of Ω , neither our numerical simulation nor the family of statistical states of the energy–enstrophy theory allow for the most basic pattern in channel flow, namely uniform constant flow.

4.1. Spin-up from zero

As in the previous section we set the viscosity to $\nu = 0.01$ and bombard the flow, initially at rest, with localized vortices of like negative sign and constant amplitude $|A| = 1$. In figure 12 we display snapshots of the potential vorticity during initial and later stages in the simulation, $t = 0, 1, 5, 10, 50, 2000$. Again at $t = 0$ the single small vortex added *ab initio* is clearly

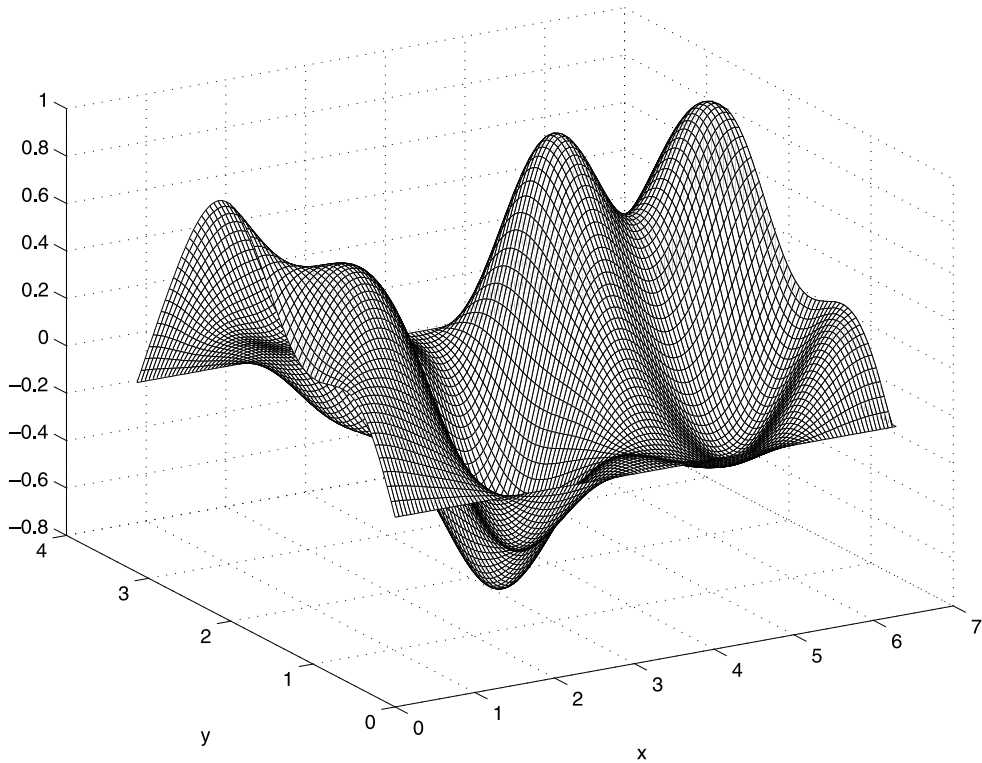


Figure 11. Random topography in the channel. The contours of topographic height are shown in the top left-hand frame of figure 12.

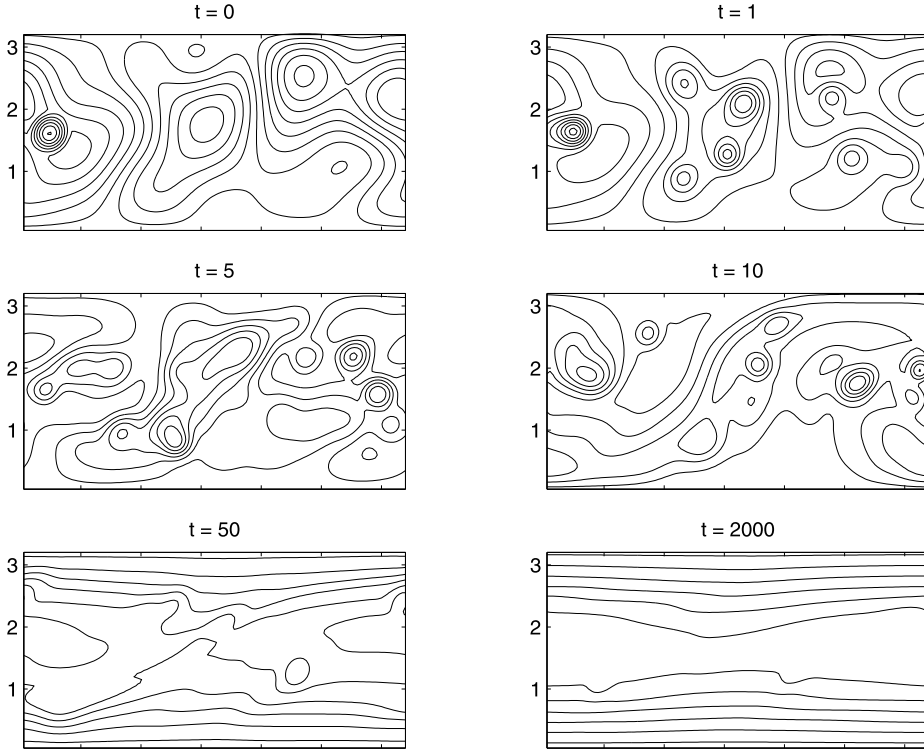


Figure 12. Snapshots of the potential vorticity at $t = 0, 1, 5, 10, 50, 2000$, during spin-up from zero in the channel, with $H = 1$ and $\nu = 0.01$.

visible against the contour lines of the topography. Although initial stages of the flow are strongly perturbed, the flow rapidly develops two large vortices in opposite directions, which correlate with the dominant topographic features. Under the incessant bombardment with small vortices, the flow accelerates further and changes its topology as the counterclockwise vortex in the centre is torn apart and a large-scale shear flow emerges around $t = 50$. This shear flow configuration remains stable to small-scale perturbation until $t = 500$, when the flow reaches a quasi-equilibrium state.

Despite the radical change in the flow topology, shown in figure 12, the crude closure rapidly bridges over the initial turbulent stages and predicts the emergence of a shear flow with the same accuracy as for flow in the basin, with relative errors in the velocity below 2% and in the vorticity of around 4%. Final values of the velocity lie around $|\vec{v}| = 8.5$, which corresponds approximately to a Reynolds number of $Re = 5400$. The lower two frames in figure 13 display the correlation and both Λ_ω and Λ_q , again during the initial stages of the simulation until $t = 50$. We note the very poor correlation of the flow with the macrostates up to $t = 10$, paralleled by very large values in Λ_ω and Λ_q , which demonstrate the strong vortical activity in the small scales. As the energy cascades from smaller to larger scales, the ratio of enstrophy to energy diminishes and coherent structures appear in the evolving flow, which eventually stabilizes into a large-scale shear flow configuration.

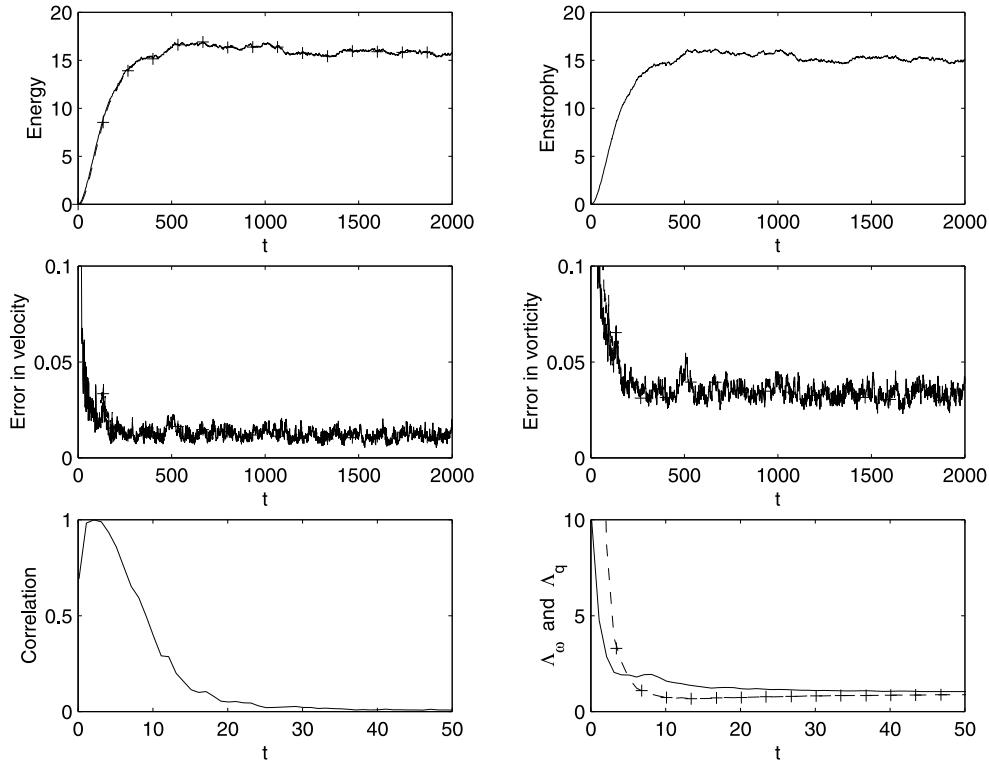


Figure 13. Comparison with crude closure dynamics during spin-up from zero in the channel, with $H = 1$ and $\nu = 0.01$. Top left, energy E (—) and predicted energy \bar{E} (+); top right, enstrophy \mathcal{E} ; middle left, relative errors in matched velocity $\text{Err}(\vec{v}, \vec{v}^*)$ (—) and predicted velocity $\text{Err}(\vec{v}, \bar{\vec{v}})$ (+); middle right, relative errors in matched potential vorticity $\text{Err}(q, q^*)$ (—) and predicted potential vorticity $\text{Err}(q, \bar{q})$ (+); bottom left, correlation $\text{Corr}(q, \psi)$; bottom right, Λ_ω (—) and Λ_q (+).

4.2. Forcing by alternating oppositely signed vortices

Again we attempt to push the crude closure to the limits of statistical theory and set $\nu = 0$. The initial flow configuration corresponds to the macrostate defined by $\mu = -\frac{1}{2}$. By strongly perturbing the flow with random vortices of alternating opposite sign, we attempt to push the flow away from statistical equilibrium. The small smoothed vortices all have constant amplitude equal to 10% of the initial maximal relative vorticity. Figure 14 displays snapshots of the potential vorticity at times $t = 0, 400, 800, 2000$. Under the incessant bombardment with small smoothed vortices, a counterclockwise vortex concentrates in the centre of the channel around $t = 400$, to be destroyed again by $t = 2000$. By that time the contour lines of the dominant vortex have lost their initially smooth character and appear tightly packed.

The rough nature of the flow is apparent from the slow but steady increase in Λ_ω and Λ_q , shown in figure 15, while the maximal potential vorticity triples over the entire simulation. The increase in Λ_q demonstrates the absence of an inverse energy cascade. Indeed, the small vortices added by the random forcing accumulate in the smaller scales of the flow and result in a fivefold increase in the enstrophy, while we observe little change in the energy. Despite the poor correlation with statistical states, with relative errors in the velocity as high as 30%, the crude closure algorithm tracks the evolution of the energy within a few per cent.

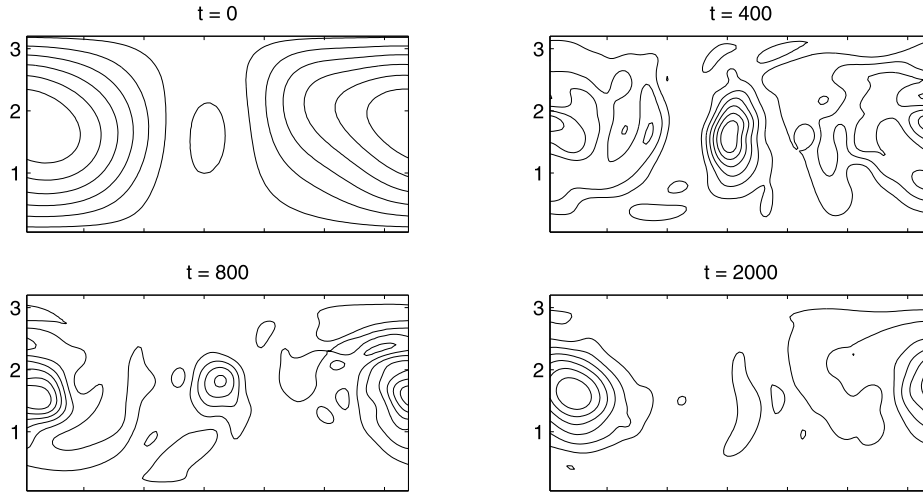


Figure 14. Snapshots of the potential vorticity at $t = 0, 400, 800, 2000$, in the channel during bombardment with localized vortices of alternating sign and amplitude equal to 10% of initial maximal vorticity.

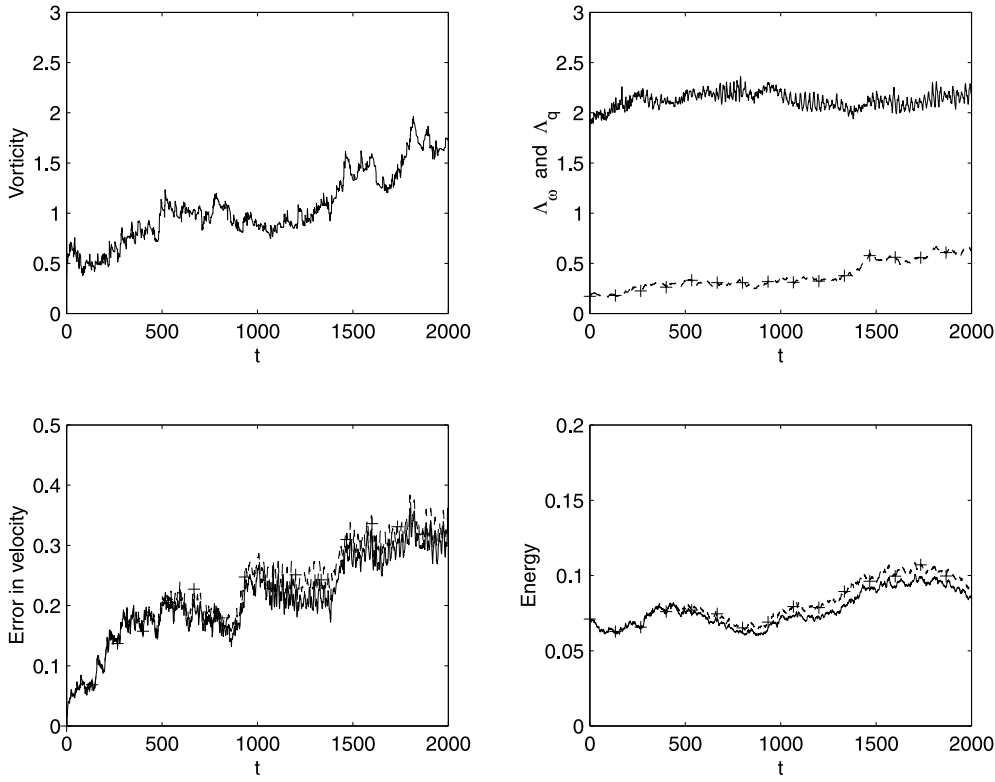


Figure 15. Comparison with crude closure dynamics during bombardment with localized vortices of alternating sign and amplitude equal to 10% of initial maximal vorticity. Top left, maximal potential vorticity $|q|_{\max}$; top right, Λ_ω (—) and Λ_q (+); bottom left, relative errors in matched velocity $\text{Err}(\vec{v}, \vec{v}^*)$ (—) and predicted velocity $\text{Err}(\vec{v}, \bar{\vec{v}})$ (+); bottom right, energy E (—) and predicted energy \bar{E} (+).

We omit showing the results from a series of numerical experiments in a doubly periodic geometry over a random topography, as they essentially corroborate our results from sections 3 and 4.

5. Layered two-mode topography in the channel

In this final section we restrict ourselves to the following layered two-mode topography in the channel:

$$h(x, y) = H\left(\frac{1}{2}\sin y + \sin(2y)\right). \quad (48)$$

This peculiar topography differs from the previous random topography (46) in two ways: first, it is layered, that is $h = h(y)$; second, in contrast to the smooth decay of Fourier coefficients of h in (46), here the second Fourier mode clearly dominates over the first mode. In general, the performance of the crude closure for flow over layered topography hardly differs from that over random topography studied in section 4. For instance, if we set $\nu = 0.01$ and $H = 1$, as in section 4.1, and spin-up the flow from zero with like-signed vortices of amplitude $|A| = 1$, both random (layered) topography, defined by (46) with $h = h(y)$, and the above two-mode topography lead to similar results. Indeed, in both cases the crude closure predicts the eventual final state of a shear flow, with relative errors in velocity below 10% for flow over two-mode topography and around 3% for flow over random topography. We refrain from showing these results, which simply corroborate the findings from our previous study. Instead, we shall devise special flow situations over two-mode topography at low energy, which illustrate the shortcomings of the crude closure based on the energy–enstrophy theory. Although the flows considered in this section are somewhat atypical and contrived, they demonstrate the potential benefit to be gained from the use of more sophisticated statistical theories, such as the Langevin theory discussed in section 2.3.

5.1. Failure of the crude closure

We now describe a special low-energy dynamic transition of the flow over layered two-mode topography, which the crude closure based on the energy–enstrophy theory is unable to predict. We let the topography be given by (48) with $H = 1$ and set the initial conditions to the steady state defined by (15) with $\mu = -0.5$. Since the topography is layered and the mean-field equation is linear, the initial condition as well as any other steady state is necessarily layered. Hence the initial flow, shown in figure 16, is a shear flow with slightly negative circulation. We set the viscosity to $\nu = 0.01$ and choose the amplitude of the forcing $|F| = 0.15$, about 10% of the initial maximal vorticity, so that the flow remains in a low-energy state, $E = O(0.1)$. Under the constant bombardment with small clockwise vortices, the energy decays until $t = 20$ but then increases to reach a steady value around 0.2, while a clockwise vortex emerges in the upper half of the channel. Although the crude closure predicts the initial decrease in energy, it fails to predict the subsequent increase. The crude closure with only two layered modes attempts to approximate the exact solution with a strong emerging large-scale vortex. During this dynamic transition from a layered to a vortical flow configuration, we observe a large, 50-fold increase in Λ_q . Since the family of steady states is restricted to zonal shear flows, the crude closure cannot accommodate the emerging vortex. A possible remedy may be the use of a crude closure based on more sophisticated statistical theories, such as the Langevin theory discussed in section 2.3, which yield a richer family of statistical states not restricted to zonal shear flows.

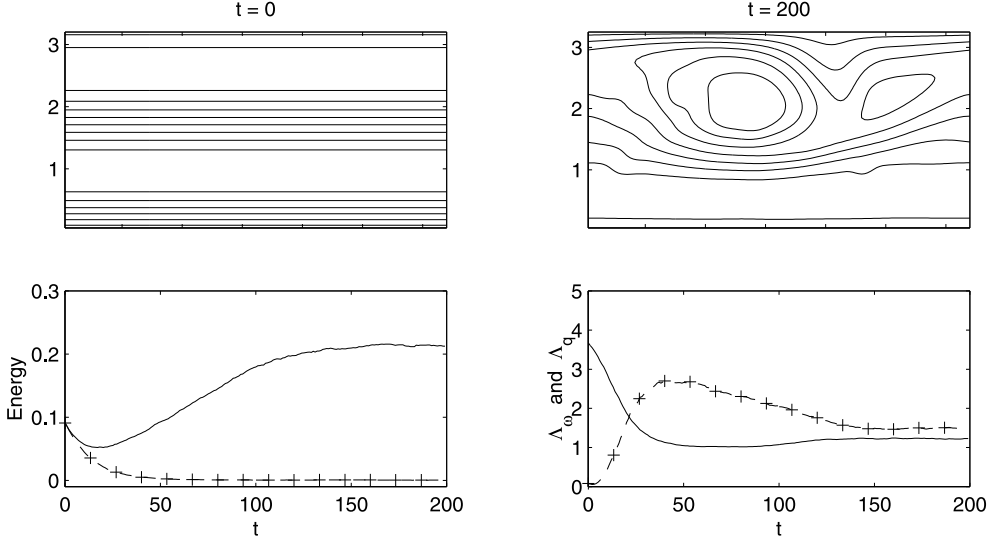


Figure 16. Comparison with crude closure dynamics during bombardment with clockwise vortices of amplitude equal to 12% of initial maximal vorticity, with $\mu_0 = -0.5$, over tall, layered, two-mode topography. Top, snapshots of potential vorticity at $t = 0$ and $t = 200$; bottom left, energy E (—) and predicted energy \bar{E} (+); bottom right, Λ_ω (—) and Λ_q (+).

5.2. Langevin statistical theories

To demonstrate the potential benefit from using more complex statistical theories, we choose a special situation for which the mean-field potential vorticity, q^* , of the Langevin statistical theory is not a zonal but instead a vortical flow. Again we set h to the layered two-mode topography in (48), but with a smaller amplitude $H = 0.1$. The initial flow configuration is set to the entropy maximizer, q^* , which results from the Langevin theory for the special parameter choice $E = 0.28$, $\Gamma = -0.34$, $Q_+ = 0.48$ and $Q_- = -1.67$ (see section 2.4). It consists of a large vortex rotating clockwise, with a tight boundary (shown in figure 17). Both the forcing and the dissipation are identical to the previous case, $|F| = 0.15$ and $\nu = 0.01$. Under the constant bombardment with like-signed, small, clockwise vortices, a background shear rapidly appears which tears apart the initial vortex. By $t = 100$ the vortex has completely disintegrated and the flow remains in a shear flow configuration for all time. Despite the inability of the energy–enstrophy theory to accommodate the initial vortex, the crude closure easily predicts the increase and long-term evolution of the energy as the flow stabilizes in a shear flow configuration, with relative errors in the velocity around 5%. Both Λ_ω and Λ_q rapidly reach their final values close to one.

Finally, we consider the same initial flow configuration but with $\nu = 0$ and bombard the flow with alternating opposite-signed vortices of amplitude equal to 5% of the maximal initial vorticity. Here the flow remains in a vortical configuration over the entire time interval until $t = 1000$. The crude closure predicts the evolution of the energy without difficulty, despite relative errors in the velocity of around 50% due to the inability of the energy–enstrophy theory to accommodate a vortex over layered topography. The vortex shifts about the channel, as shown in the top left-hand frame of figure 18. Moreover, its overall appearance evolves as its contours become smoother and stretched out in the zonal direction. Why does the vortex translate at a constant speed rather than remain steady in the channel? For the special layered

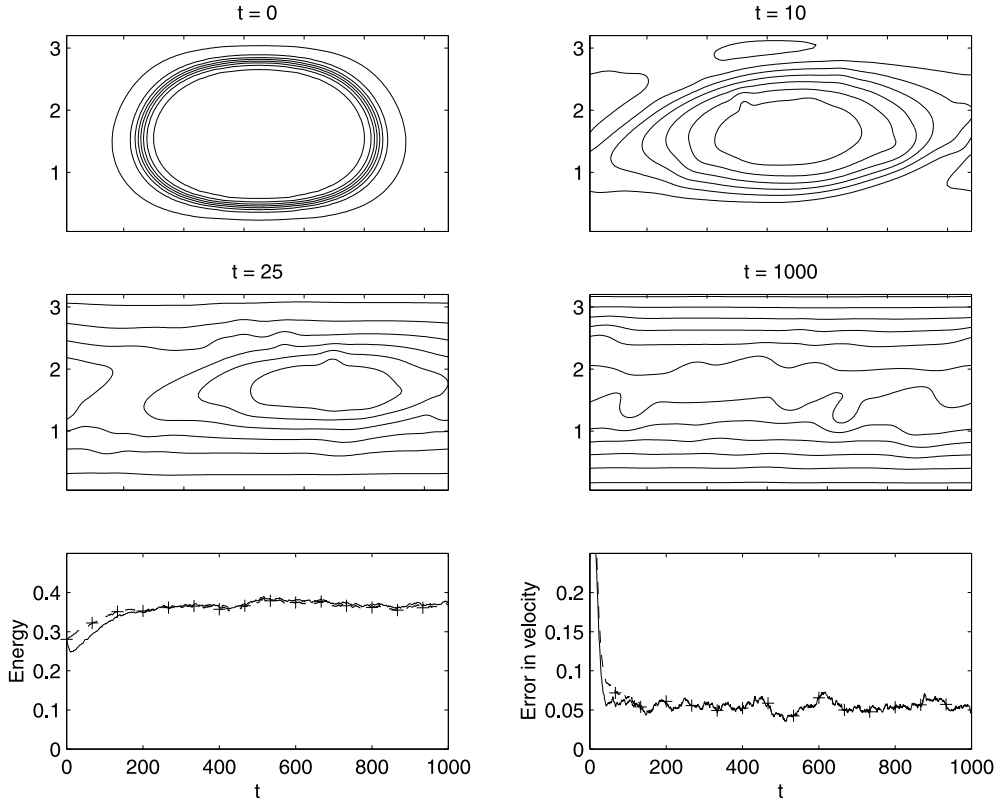


Figure 17. Comparison with crude closure dynamics during bombardment with clockwise vortices of amplitude equal to 8% of initial maximal vorticity, with low amplitude, layered, two-mode topography and the initial conditions set to a Langevin entropy maximizer. Top, snapshots of potential vorticity at $t = 0$ and $t = 10$; middle, snapshots of potential vorticity at $t = 25$ and $t = 1000$; bottom left, energy E (—) and predicted energy \bar{E} (+); bottom right, relative errors in matched velocity $\text{Err}(\vec{v}, \vec{v}^*)$ (—) and predicted velocity $\text{Err}(\vec{v}, \vec{v})$ (+).

topography considered in this section, solutions are translation invariant in x and the inviscid dynamics has an additional conserved quantity associated with the mean motion, the impulse,

$$I = \oint x q.$$

The impulse in the emerging translating vortex is essentially constant in this time interval and yields the slow propagation speed depicted at $t = 200$ and 670 in figure 18.

Now we check the consistency (see section 2.3) of the Langevin statistical theory at the time $t = 670$. With the current values of the time-dependent flow $E = 0.30$, $\Gamma = -0.48$, $Q_+ = 0.21$ and $Q_- = -2.31$, we compute the entropy maximizer of the Langevin statistical theory. The corresponding mean-field potential vorticity, q^* , is shown in the lower right-hand frame of figure 18 and compares favourably with the flow at $t = 670$, shown above it. In particular, we note how the contours of q^* are also smooth and slightly stretched in the zonal direction. The relative error in potential vorticity is 19%, a clear improvement over the 70% relative error in the layered solution of the energy–enstrophy statistical theory. In this simplified consistency check, we have ignored the impulse constraint in applying the Langevin statistical theory at a given time and obtained reasonably accurate results. This constraint is readily

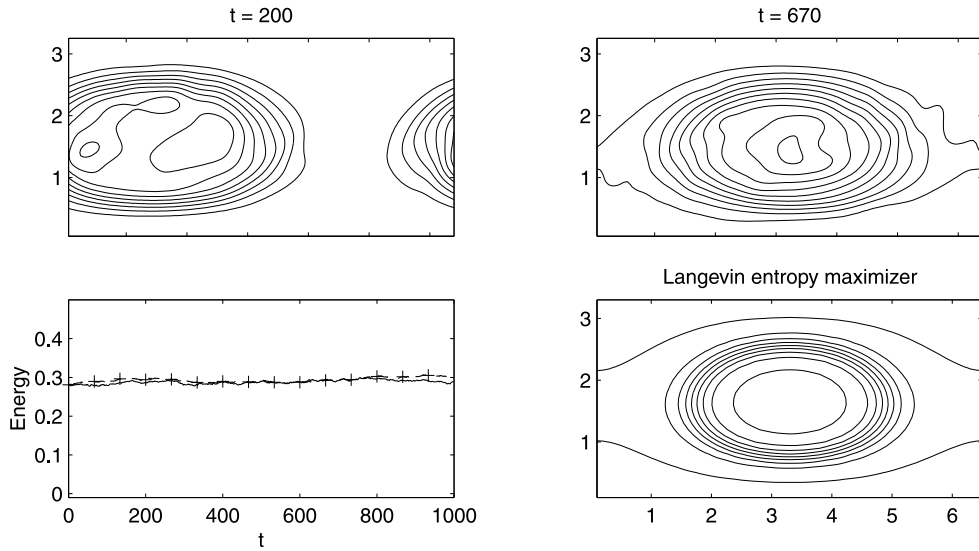


Figure 18. Evolution of Langevin mean-field state during bombardment with localized vortices of alternating sign and amplitude equal to 5% of initial maximal vorticity, with low amplitude, layered, two-mode topography and the initial conditions set to the Langevin entropy maximizer (see figure 18). Top, snapshots of potential vorticity at $t = 200$ and $t = 670$; bottom left, energy E (—) and predicted energy \tilde{E} (+); bottom right, Langevin entropy maximizing mean-field potential vorticity, q^* , with E , Γ , Q and \tilde{Q} matched from the exact solution at $t = 670$ (top right). Note, contour lines are at identical levels in the above three frames.

incorporated in the statistical theory [13] and would be needed in order to attempt to describe the full transient behaviour by a crude closure algorithm. Although we have only verified the consistency of the Langevin theory, the crude closure algorithm could be extended to predict the evolution of the two additional parameters Q_+ and Q_- . This last example demonstrates the potential benefit resulting from the use of more complex statistical theories, such as the Langevin theory.

6. Concluding discussion

The equilibrium states of few-constraint statistical theories have proved to be reasonably robust to small-scale forcing in a variety of geometries and for a wide range of underlying topography. By using these equilibrium statistical states, we have devised a simple procedure, the crude closure algorithm, which predicts within a small error margin the general trend of large-scale features of the flow as it evolves under intense, small-scale forcing. Systematic comparison with the full numerical solution demonstrates that the one-parameter crude closure based on the energy–enstrophy theory generally tracks with high accuracy the evolution of bulk features of the flow, such as the energy. We have tested the crude closure for random and layered topography in three types of geometry: the basin, the channel and periodic geometry. Typically the crude closure predicts the evolution of the energy to within a few per cent, while relative errors in the velocity range from 5% to 10%. An exception to this situation, documented in sections 4 and 5, occurs when the enstrophy-to-energy ratio is large or increases rapidly in time. As demonstrated in section 5, more sophisticated statistical theories, as discussed in section 2.3, can be used to enrich the family of statistical states by including additional conserved quantities

and prior distributions. Then the resulting crude closure dynamics accommodate a wider range of flow regimes at the expense of a more complicated numerical procedure. The ratio of enstrophy to energy, Λ_q , has proved a reliable indicator for the performance of the crude closure, with improved performance at lower values. Large values of Λ_q indicate little or no inverse energy cascade and as a result no emergence of large-scale coherent structures. Although strongly perturbed flows often produce large relative errors in velocity, the crude closure algorithm is able to track the evolution of bulk features of the flow quite accurately, as long as Λ_q is not too big. Large values of Λ_q correspond either to flow where all the energy resides in the small scales or to creeping flow dominated by topography, where little mixing occurs. Furthermore, whenever the flow crosses a rough transition where Λ_q is large and the correlation poor, the crude closure is able to predict the general trend of bulk features and recover its original accuracy. However, examples of failure of the crude closure to track the energy accurately through regimes with large Λ_q are documented in section 5.1.

Given the encouraging results presented in this paper involving crude dynamical closure modelling based on large-scale statistical theory, it is important to point out some limitations of the approach. The most important limitation involves the requirement of strong mixing or ergodicity of the flow field. This issue was circumvented here through the use of a simple geometry and small-scale random forcing with an essentially uniform distribution of locations. For more realistic geophysical flows involving large-scale forcing and the beta effect, distinct mixing regions can emerge through a combination of these effects [1, 24]. It is very interesting to devise a crude dynamic closure based on statistical theories which can account for these new physical effects. The authors are currently pursuing these issues and will report on them elsewhere in the near future.

Acknowledgments

The authors would like to thank M DiBattista for providing them with computer software to calculate the Langevin statistical states in section 5. The research of AM is partially supported by grants NSF DMS-9596102-001, NSF DMS-9625795, ONR N00014-96-00443 and ARO DAAG55-98-1-0129.

References

- [1] Holloway G 1986 Eddies, waves, circulation and mixing: statistical geofluid mechanics *Ann. Rev. Fluid Mech.* **18** 91–147
- [2] McWilliams J C 1984 The emergence of isolated coherent vortices in turbulent flow *J. Fluid Mech.* **146** 21–43
- [3] Kraichnan R H 1975 Statistical dynamics of two-dimensional flow *J. Fluid Mech.* **67** 155–75
- [4] Salmon R, Holloway G and Henderschott M C 1976 The equilibrium statistical mechanics of simple quasi-geostrophic models *J. Fluid Mech.* **75** 691–703
- [5] Montgomery D and Joyce G 1974 Statistical mechanics of negative temperature states *Phys. Fluids* **17** 1139–45
- [6] Pointin Y B and Lundgren T S 1976 Statistical mechanics of two dimensional vortices in a bounded container *Phys. Fluids* **10** 1459–70
- [7] Kraichnan R H and Montgomery D 1980 Two-dimensional turbulence *Rep. Prog. Phys.* **43** 548–619
- [8] Caglioti E, Lions PL, Marchioro C and Pulvirenti M 1992 A special class of stationary flows for two-dimensional Euler equations: a statistical mechanics description *Commun. Math. Phys.* **143** 501–25
- [9] Miller J 1990 Statistical mechanics of Euler equations in two dimensions *Phys. Rev. Lett.* **65** 2137–40
- [10] Miller J, Weichman P B and Cross M C 1992 Statistical mechanics, Euler's equation and Jupiter's red spot *Phys. Rev. A* **45** 2328–59
- [11] Robert R 1991 A maximum entropy principle for two-dimensional Euler equations *J. Stat. Phys.* **65** 531–53
- [12] Turkington B 1999 Statistical equilibrium measures and coherent states in two-dimensional turbulence *Commun. Pure Appl. Math.* **52** 781–809

- [13] DiBattista M T, Majda A J and Turkington B 1998 Prototype geophysical vortex structures via large-scale statistical theory *Geophys. Astrophys. Fluid Dynam.* **89** 235–83
- [14] Majda A and Holen M 1997 Dissipation, topography and statistical theories for large scale coherent structure *Commun. Pure Appl. Math.* **50** 1183–234
- [15] Grote M J and Majda A J 1997 Crude closure dynamics through large scale statistical theories *Phys. Fluids* **9** 3431–42
- [16] Holloway G and Eby M 1993 Hybrid statistical mechanics—ocean circulation for efficient large scale modelling *Proc. Oceans '93 (Victoria BC, Canada)* vol 1 (Piscataway, NJ: IEEE) p 323
- [17] Holloway G 1992 Representing topographic stress for large-scale ocean models *J. Phys. Oceanography* **22** 1033–46
- [18] Carnevale G and Frederiksen J 1987 Nonlinear stability and statistical mechanics of flow over topography *J. Fluid Mech.* **175** 157–81
- [19] Bretherton F B and Haidvogel D B 1976 Two-dimensional turbulence above topography *J. Fluid Mech.* **78** 129–54
- [20] Wang J and Vallis G 1994 Emergence of Fofonoff states in inviscid and viscous ocean circulation models *J. Marine Res.* **52** 83–127
- [21] Treguier A 1989 Topographically generated steady currents in barotropic turbulence *Geophys. Astr. Fluid Dynam.* **47** 43–68
- [22] Pedlosky J 1986 *Geophysical Fluid Dynamics* (New York: Springer)
- [23] Turkington B and Whitaker N 1996 Statistical equilibrium computations of coherent structures in turbulent shear layers *SIAM J. Sci. Comput.* **17** 1414–33
- [24] Griffa A and Salmon R 1989 Wind-driven ocean circulation and equilibrium statistical mechanics *J. Marine Res.* **47** 457–92